IEEE Access
Multidisciplinary ⋮ Rapid Review ⋮ Open Access Journal

Received June 18, 2020, accepted August 19, 2020, date of publication August 26, 2020, date of current version September 9, 2020.

Digital Object Identifier 10.1109/ACCESS.2020.3019517

Watermarking of HDR Images in the Spatial Domain With HVS-Imperceptibility

KARINA RUBY PEREZ-DANIEL[1], (Member, IEEE), FRANCISCO GARCIA-UGALDE[2], AND VICTOR SANCHEZ[3], (Member, IEEE)

[1]Engineering Faculty, Universidad Panamericana (UP), Mexico 03920, Mexico
[2]Engineering Faculty, National Autonomous University of Mexico (UNAM), Mexico 04510, Mexico
[3]Department of Computer Science, University of Warwick, Coventry CV4 7AL, U.K.

Corresponding author: Karina Ruby Perez-Daniel (kperezd@up.edu.mx)

This work was supported in part by the National Autonomous University of Mexico (UNAM) through the Office for Academic Staff Affairs (DGAPA) Postdoctoral Scholarship Program, in part by the Research Project under Grant PAPIIT-IT101119, in part by the European Union Horizon 2020 Project Identity under Project 690907, and in part by the Universidad Panamericana.

ABSTRACT This paper presents a watermarking method in the spatial domain with HVS-imperceptibility for High Dynamic Range (HDR) images. The proposed method combines the content readability afforded by invisible watermarking with the visual ownership identification afforded by visible watermarking. The HVS-imperceptibility is guaranteed thanks to a Luma Variation Tolerance (LVT) curve, which is associated with the transfer function (TF) used for HDR encoding and provides the information needed to embed an imperceptible watermark in the spatial domain. The LVT curve is based on the inaccuracies between the non-linear digital representation of the linear luminance acquired by an HDR sensor and the brightness perceived by the Human Visual System (HVS) from the linear luminance displayed on an HDR screen. The embedded watermarks remain imperceptible to the HVS as long as the TF is not altered or the normal calibration and colorimetry conditions of the HDR screen remain unchanged. Extensive qualitative and quantitative evaluations on several HDR images encoded by two widely-used TFs confirm the strong HVS-imperceptibility capabilities of the method, as well as the robustness of the embedded watermarks to tone mapping, lossy compression, and common signal processing operations.

INDEX TERMS HDR, invisible watermarking, visible watermarking, LVT curve, HVS-imperceptibility.

I. INTRODUCTION

HDR images are characterized by a wide range of visible luminance values that can accurately represent the radiance of the scene, ranging from direct sunlight to faint starlight. Thanks to its floating-point representation, this type of imaging data can depict more colors and cover a wider range of intensity values than its Standard Dynamic Range (SDR) counterpart. Acquiring, storing, and displaying HDR images is possible thanks to the use of Transfer Functions (TFs), which perform the mapping from the linear light components of the scene, to a non-linear digital signal, and eventually to a linear luminance signal to be radiated by an HDR screen. TFs can then emulate the Human Visual System (HVS) by using non-linear operations to quantize the values representing the visible luminance with minimal subjective distortions.

The associate editor coordinating the review of this manuscript and approving it for publication was Claudio Cusano.

As HDR images become widespread, their vulnerability to piracy, unauthorized distribution, modifications, and illegal copying is expected to increase. HDR imaging piracy may result in significant losses to the economy, harming content production firms and distribution companies. In the U.S. alone, a recent study estimates that global online piracy costs the economy at least $29.2 billion in lost revenue each year [1].

Watermarking is an effective tool not only for media ownership identification but also for auxiliary information delivery. The watermark, or auxiliary information, is usually embedded in the cover media as barcodes, Quick Response (QR) codes, logos, or copyright patterns. This embedded information may be visible or invisible depending on the watermarking process. It is well-known that invisible watermarking does not seriously degrade the visual quality of the cover media by performing the embedding process after a transformation, e.g., in the frequency domain. However, this type of watermarking usually requires the exchange of private

keys or extra information about the embedding process to retrieve the watermark. Conversely, visible watermarking allows to visually assert the media's ownership without the need for such keys or extra information. This is usually achieved by performing the embedding process in the spatial domain; e.g., by altering pixel values. Visible watermarking is desirable when the copyrighted material is disseminated over channels where piracy control is not possible, e.g., the Internet, as the visible watermark can make the final user immediately aware of the media's ownership. However, this type of watermarking inevitably degrades the visual quality of the cover media.

To leverage the advantages of visible and invisible watermarking for HDR imaging, we propose a watermarking method in the spatial domain with HVS-imperceptibility capabilities. Our method, hereinafter called High Dynamic Range - Imperceptible Watermarking, (HDR-IW) provides an easy way to recognize the media's ownership without the need for exchanging keys or any extra information about the embedding process, while minimizing the visual distortion that can be perceived by the HVS. The proposed method is based on the Unseen Visible Watermarking (UVW) technique [2], [3] and extends our work in [4]. Differently from the UVW technique, which embeds copyright information in the spatial domain of SDR regions with low visibility, the HDR-IW method embeds imperceptible watermarks in the spatial domain by exploiting the inaccuracies among the non-linear digital representation of the linear luminance acquired by an HDR sensor, the linear luminance radiated by an HDR screen by means of a TF, and the brightness perceived by the HVS from the displayed luminance. The latter is achieved by using the information provided by a Luma Variation Tolerance (LVT) curve [4]. This paper extends and complements [4] as follows:

1) The technical details and computation of the LVT curve are explained in detail for the two TFs widely-used to encode HDR images. The LVT is a core component to determine the maximum variations in luma codes that a pixel can suffer before the changes can be perceived by the HVS according to the TF used for encoding.
2) An embedding region (ER) selection process is introduced to find the region with the highest tolerance to luma code variations according to the corresponding LVT curve.
3) A novel embedding payload metric is introduced to measure the embedding payload of the HDR-IW method by accounting for the characteristics of the HDR image and the corresponding LVT curve and TF.

The watermarks embedded by the HDR-IW method in the spatial domain are imperceptible to the HVS as long as the TF is not altered or the normal calibration and colorimetry conditions of the HDR screen remain unchanged. Hence, these watermarks can be easily identified without the need for private keys or any additional information about the embedding process.

We evaluate the proposed HDR-IW method for the embedding of binary watermarks in terms of embedding payload, imperceptibility (qualitatively and quantitatively), robustness to tone-mapping operations (TMOs), which are widely used to display HDR images on SDR screens, lossy compression [5]–[7] and other common signal processing operations. To the best of our knowledge, there are no other watermarking methods for HDR images that also embed information in the spatial domain in an imperceptible manner. However, we compare the imperceptibility capabilities and robustness of the HDR-IW method with those of two invisible watermarking methods that operate in the frequency domain, [8], [9].

The rest of the paper is organized as follows, Section II reviews comparable watermarking methods for HDR images that embed invisible watermarks after transforming the cover media. Section III briefly describes the HDR acquisition and encoding process. Section IV explains in detail the HDR-IW method. Section V presents and discusses the performance evaluation results. Finally, Section VI concludes this work.

II. RELATED WORK

Although SDR watermarking is a mature area that has been extensively explored both in the spatial and frequency domains, HDR watermarking is still in the early stages. In the last few years, however, important watermarking methods for HDR imaging that embed invisible watermarks after transforming the cover media have been proposed. These methods can be classified into two main groups. The first group includes methods that embed the watermark after applying a frequency transformation. For example, Bakhsh and Moghaddam [8] employ an artificial bee colony algorithm to find the best region to embed a binary watermark in the first-level approximation sub-band of the Discrete Wavelet Transform (DWT). Maiorana and Campisi [9] present a blind-detectable multi-bit watermarking method that uses the DWT of the Just Noticeable Difference (JND)-scaled representation of the HDR image for embedding purposes, as well as a contrast sensitivity function to modulate the watermark intensity in each DWT sub-band according to its scale and orientation. Guerrini *et al.* [10] present a blind-detectable one-bit watermarking method that uses the approximation sub-band of the DWT of the LogLUV color space. Autrusseau and Goudia [11] propose a non-linear hybrid method that combines additive and multiplicative watermarking. The embedding process is done in the DWT domain of the RGB radiances of an RGBe-encoded HDR image. The work in [12] exploits the properties of the Radon-Discrete Cosine Transform (R-DCT) to derive an image representation whose coefficients can be watermarked with an insignificant effect on the visual quality. In [13], the authors propose a watermarking method robust to TMOs by successively performing a non-subsampled contourlet transform and singular value decomposition to extract the structural information that is invariant to tone-mapping.

The second group of HDR watermarking methods includes those that embed the watermark after applying a color

decomposition or filtering process. The work in [14] proposes a method based on feature map extraction by means of the Tucker decomposition. This method divides an HDR RGB color image into the three color channels so that three feature maps are extracted. The method then embeds a watermark in the feature map that contains most of the image's energy. In [15], the authors decompose an HDR image into multiple SDR images by means of a bracketing process. Each SDR image is watermarked with a random key before being merged to produce the final watermarked HDR image. In [16], the authors propose a blind-detectable watermarking method that uses bilateral filtering to extract the small scale and texture parts of the HDR image, also known as the blue component of the detail layer. The watermark is embedded in this blue component to minimize quality degradations.

In summary, the previous watermarking methods have been shown to achieve strong performance. However, they may require the deployment of specific watermark detection and extraction modules. For example, the methods in [8], [16], and [10] require an explicit exchange of private keys to detect and extract the watermark. Although embedding watermarks in the spatial domain eliminates the trouble of deploying an extraction module, such an embedding technique is seldom explored because the embedded watermarks are visible and hence defeat the goal of providing a high-quality and realistic visual experience through HDR imaging. To the best of our knowledge, no watermarking method in the spatial domain with HVS-imperceptibility for HDR imaging has been previously proposed. Such methods have only been proposed for SDR images. For example, [17] and [18] propose to exploit the cover media's color histogram to embed the watermark in the spatial domain with HVS-imperceptibility. The method in [19], on the other hand, uses a JND criterion for embedding in the spatial domain, the DCT to share extraction parameters, and a binarization function for extraction. Although these watermarking methods have HVS-imperceptibility capabilities, they are not suitable for HDR images because of the color and visibility ranges of SDR images differ from those of HDR images, which comes as a consequence of using distinct TFs to encode the luminance and color information [9].

III. HDR IMAGING

The abbreviations and acronyms used in this work are defined in Table 1.

Acquiring luminance from a scene in the form of an HDR image requires to first map the scene's linear luminance to a non-linear digital signal in the form of code values. This mapping is done through an opto-electronic transfer function (OETF). To display HDR images, the code values are mapped back to a linear luminance signal to be radiated by an HDR screen by means of an electro-optical transfer function (EOTF).

TABLE 1. List of Abbreviations and Acronyms.

Abbreviation	Description	Abbreviation	Description
HDR	High Dynamic Range	LVT	Luma Variation Tolerance
TF	Transfer Function	HVS	Human Visual System
SDR	Standard Dynamic Range	QR	Quick Response
HDR-IW	High Dynamic Range - Imperceptible Watermarking	UVW	Unseen Visible Watermarking
TMO	Tone Mapping Operation	CS	Contrast Sensitivity
OETF	Opto-Electronic Transfer Function	EOTF	Electro-Optical Transfer Function
PQ	Perceptual Quantization	HLG	Hybrid Log-Gamma
HDR-VDP-2	HDR Visual Difference Predictor	MOS	Mean Opinion Score
mPSNR	multi-exposure Peak Signal to Noise Ratio	MSE	Mean Square Error
QP	Quantization Parameter	BER	Bit Error Rate

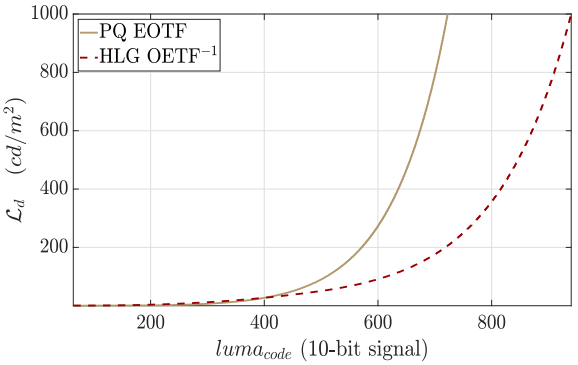

FIGURE 1. Mapping of luma codes to display luminance by different EOTFs.

Two TFs are currently used for HDR images: the Perceptual Quantization (PQ) EOTF and the Hybrid Log-Gamma (HLG) OETF. The PQ EOTF, also known as the SMPTE ST.2084 standard [20], maps 10-bit luma codes, $luma_{code} \in [0, 2^{10} - 1]$, to display luminance $\mathcal{L}_d \in [10^{-4}, 10^4]\ cd/m^2$. This EOTF is an absolute, display-referred TF, as the maximum possible $\mathcal{L}_d$ value depends on the screen's display capabilities. However, this TF maps each luma code to the same absolute luminance value in every screen. HDR images encoded by the PQ EOTF are not directly backward compatible with SDR screens. Conversely, the HLG OETF preserves backward compatibility. This TF is a relative, scene-referred TF [21], since digital signals produced by this TF represent the intensity of the light relative to the peak output of the HDR sensor.

Ideally, a TF should be a reversible function. Unfortunately, TFs are not reversible and the mapping between linear light components and non-linear codes is lossy. Fig. 1 plots the mapping of 10-bit luma codes, $luma_{code} \in [64, 940]$, to display luminance by the two EOTFs previously discussed. For the case of the HLG TF, Fig. 1 plots the inverse of the OETF, i.e., OETF^{-1}, as the EOTF. Note that each EOTF maps the same luma code to a slightly different display luminance value. This can be best appreciated in Fig. 2.

Contrast threshold curves are commonly used to study the HVS' ability to make contrast distinctions [22], [23]. Fig. 3 shows the contrast threshold curve proposed by Hecht *et al.* [22], where the luminance, $\mathcal{L}$, is plotted from very dark to very bright conditions against the JND perceived by the HVS ($\Delta\mathcal{L}/\mathcal{L}$). The JND model in Fig. 3 shows the three regions used to describe the HVS' behaviour when detecting contrast. The *scotopic* region, $\mathcal{L} \in [10^{-6}, 10^{-3}]\ cd/m^2$, which follows the De Vries-Rose law. The *photopic* region, $\mathcal{L} \in [10, 10^8]\ cd/m^2$, which follows a relatively constant trend, i.e., the Weber-Fechner Law. And

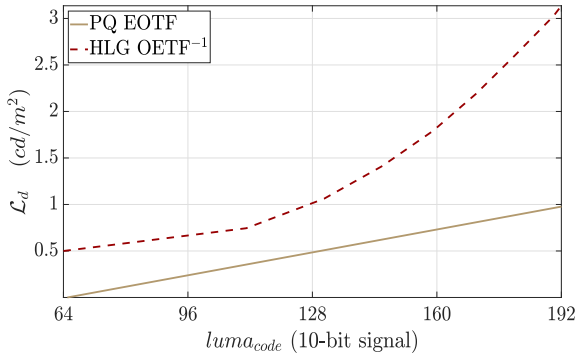

FIGURE 2. Mapping of $luma_{code} \in [64, 192]$ to display luminance by different EOTFs.

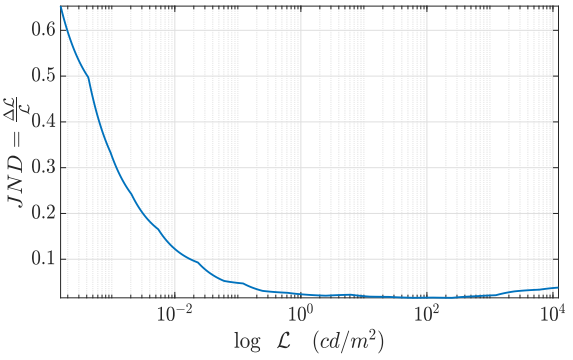

FIGURE 3. Hecht's curve modeling the HVS' relationship between contrast thresholds, $JND = \Delta\mathcal{L}/\mathcal{L}$, and luminance, $\mathcal{L}$.

the *mesopic* region, $\mathcal{L} \in (10^{-3}, 10)$ cd/m^2, which combines the characteristics of the scotopic and photopic regions. JND models like the one in Fig. 3 are used to design TFs with smooth visual transitions between consecutive luma code values. This is achieved by establishing coding steps below the threshold of visibility [24].

IV. PROPOSED HDR-IW METHOD

The HDR-IW method embeds binary watermarks in the spatial domain of the Y-channel with HVS-imperceptibility. It comprises 4 main stages, as depicted in Fig. 4 and described next.

A. LUMA VARIATION THRESHOLD CALCULATION

When an initial low luminance stimulus is given to the HVS, very large variations in such a stimulus are required for the HVS to perceive any changes, as shown in Fig. 3. Designing a TF that accurately models the HVS' response to any luminance stimulus is a challenging task. Current TFs represent a trade-off between computational complexity and accuracy of the code assignment process. This trade-off usually results in representing low luminance values with a wide range of luma codes in order to minimize visible contouring artifacts at such low luminance levels. For example, for 10-bit signals, the PQ EOTF employs 100 luma codes to represent display luminance values $\mathcal{L}_d \in [0.0001, 0.75)$ cd/m^2, 64 luma codes for $\mathcal{L}_d \in [0.75, 2)$ cd/m^2, and only 22 luma codes for $\mathcal{L}_d \in [2, 3)$ cd/m^2. Among the 100 luma codes used by this TF for $\mathcal{L}_d \in [0.0001, 0.75)$ cd/m^2, there is some redundancy that results in a significant amount of bits being wasted to encode small contrast changes that the HVS may not be capable of perceiving at such low luminance levels. A similar situation occurs with the HLG OETF^{-1}. In other words, there is a mismatch between the HVS's capacity to perceive differences in display luminance and the modeling used by an EOTF to represent display luminance as luma codes. Consequently, luma codes used to represent low display luminance values can be appropriately modified to embed a watermark in the spatial domain so it is imperceptible to the HVS. The challenge here is to determine the regions that are most tolerant to luma code variations and the maximum variation that they can tolerate before these changes can be perceived by the HVS, i.e., their luma variation threshold, denoted by ξ. For a given EOTF, we propose to compute ξ for a luma code, $luma_{code}$, based on the difference, or error, between the contrast sensitivity (CS) of the HVS and the CS modeling of an EOTF. To this end, we first determine how the luma code assignment of an EOTF changes as the display luminance, $\mathcal{L}_d$, increases linearly, and how the HVS' CS increases as $\mathcal{L}_d$ increases linearly.

1) INCREASE IN $luma_{code}$ AS $\mathcal{L}_d$ INCREASES LINEARLY

Let us recall that the end-to-end mapping of the linear light components of a real-life scene to the linear luminance values displayed by an HDR screen involves a non-linear quantization in the form of a digital signal. This means that if the luminance values displayed by an HDR screen increase in a linear trend, the corresponding luma codes do not increase linearly. To illustrate this, let us first define the increase in luma codes, $\Delta luma_{code}$, when the display luminance, $\mathcal{L}_d$, increases linearly by 1 cd/m^2, as follows:

$$\Delta luma_{code}(\mathcal{L}_d) = luma_{code}[\mathcal{L}_d + 1] - luma_{code}[\mathcal{L}_d], \quad (1)$$

where $luma_{code}[\mathcal{L}_d]$ is the luma code assigned to the display luminance value, $\mathcal{L}_d$.

Fig. 5 plots Eq. (1) for the two HDR EOTFs for $\mathcal{L}_d \in [0.5, 1000]$ cd/m^2. It is evident that when the display luminance values increase linearly by 1 cd/m^2, the luma codes do not increase linearly. Note that for the two EOTFs, Eq. (1) follows a trend similar to that shown in Fig. 3, especially for low display luminance values. In other words, there is a wide range of luma codes available to represent low $\mathcal{L}_d$ values compared to the narrow range available for large $\mathcal{L}_d$ values.

2) INCREASE IN THE HVS' CS as $\mathcal{L}_d$ INCREASES LINEARLY

Part of the HVS' ability to discern information is attributed to its capacity to perceive differences in luminance within a field of vision [25]. Changes in luminance create a pattern of contrast that conveys the majority of visual information to the viewer. The HVS' sensitivity to detect contrast is given by the reciprocal of the JND value. The CS derived from this reciprocal, i.e., $CS = 1/JND$, is indeed the minimum perceived brightness by the HVS associated with a contrast threshold,

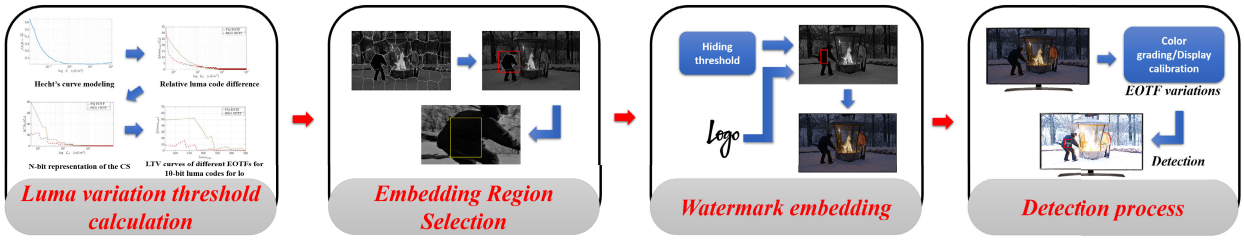

FIGURE 4. The four steps comprising the proposed HDR-IW method.

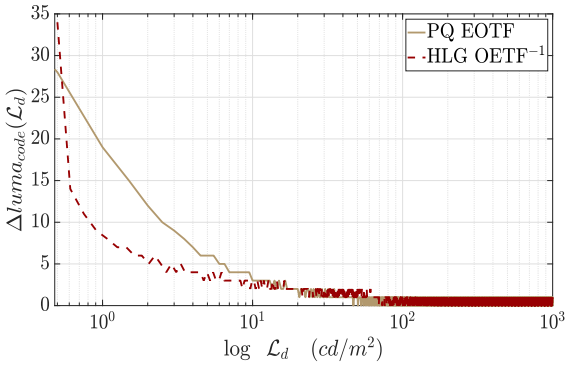

FIGURE 5. $\Delta luma_{code}(\mathcal{L}_d)$ of different EOTFs.

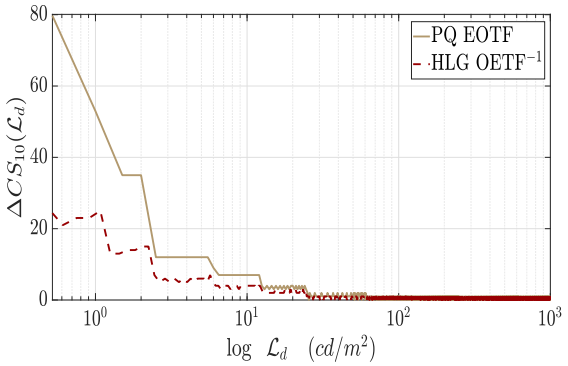

FIGURE 6. $\Delta CS_{N_{10}}(\mathcal{L}_d)$ of different EOTFs.

$\Delta\mathcal{L}/\mathcal{L}$ [26]. To appropriately compare the HVS' CS with the display luminance encoded as luma codes, we apply the same N-bit quantization used by an EOTF to the HVS' CS [27]. This N-bit quantization is given by:

$$CS_{N_{bit}} = \left[\left(219 \cdot \frac{1}{JND} + 16\right) \cdot 2^{N-8}\right], \tag{2}$$

where $[x]$ denotes the rounding operation on x.

The increase in the HVS' CS after N-bit quantization can then be measured as the increase in $CS_{N_{bit}}$ values when the display luminance increases linearly by 1 cd/m^2, as follows:

$$\Delta CS_{N_{bit}}(\mathcal{L}_d) = CS_{N_{bit}}[\mathcal{L}_d + 1] - CS_{N_{bit}}[\mathcal{L}_d], \tag{3}$$

where $CS_{N_{bit}}[\mathcal{L}_d]$ is the N-bit representation of the HVS's CS associated with the display luminance value, $\mathcal{L}_d$. Fig. 6 plots Eq. (3) for the case of 10-bit signals, i.e., $\Delta CS_{N_{bit}=10}(\mathcal{L}_d)$. Note that for the two EOTFs, Eq. (3) follows a trend similar to that shown in Fig. 5. However, there are differences between the values given by $\Delta CS_{10}(\mathcal{L}_d)$ and those given by $\Delta luma_{code}(\mathcal{L}_d)$ for the same EOTF. These differences are exploited to modify luma codes in the spatial domain in an imperceptible manner, as explained next.

3) LUMA VARIATION THRESHOLD AND THE LVT CURVE

Once the $\Delta luma_{code}$ and $\Delta CS_{N_{bit}}$ values are computed for a display luminance value, $\mathcal{L}_d$, we can define the luma variation threshold, ξ, for $\mathcal{L}_d$ as the absolute difference, or absolute error, between these two values:

$$\xi(\mathcal{L}_d) = \left|\Delta CS_{N_{bit}}(\mathcal{L}_d) - \Delta luma_{code}(\mathcal{L}_d)\right|. \tag{4}$$

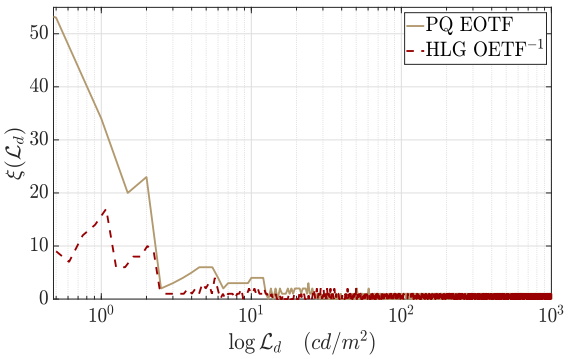

FIGURE 7. LVT curves of different EOTFs.

Fig. 7 plots $\xi(\mathcal{L}_d)$ for 10-bit signals. These curves are the LVT curves, one for each EOTF. Note that according to these LVT curves, low $\mathcal{L}_d$ values can tolerate large variations before the HVS is capable of perceiving them. This tolerance is relatively constant for all other $\mathcal{L}_d$ values. This is better appreciated in Fig. 8, which shows the LVT curves for the lowest $\mathcal{L}_d$ values plotted in Fig. 7. In this figure, one can note that for $\mathcal{L}_d$ values within the boundaries of the scotopic and mesopic regions, there exists an important discrepancy between the CS modeling used by a TF and the brightness perceived by the HVS, i.e., the HVS's CS. The greatest differences are found for $\mathcal{L}_d < 2.5$ cd/m^2, for both EOTFs.

It is important to note that the LVT curves in Fig. 7 can also be defined in terms of luma codes. Fig. 9 shows the LVT curves plotted as a function of $luma_{code}$, i.e., $\xi(luma_{code})$, for

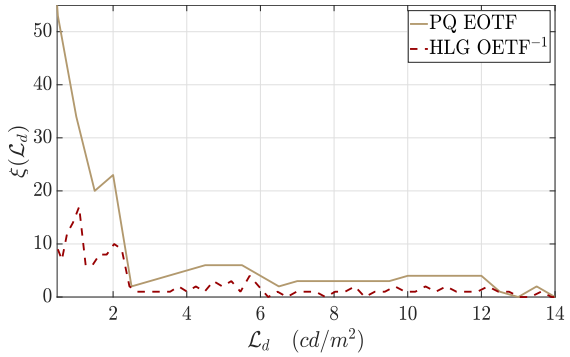

FIGURE 8. LVT curves of different EOTFs for low $\mathcal{L}_d$ values.

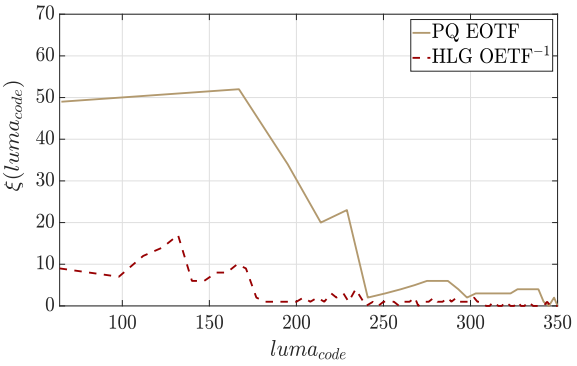

FIGURE 9. LVT curves of different EOTFs for 10-bit luma codes associated with low $\mathcal{L}_d$ values.

10-bit signals. For a PQ compatible system, one can see that a $luma_{code} = 100$ can be modified to any value $\in [75, 125]$ without being perceived by the HVS, since $\xi(100) = 50$. In the case of an HLG compatible system, a $luma_{code} = 100$ can be modified to any value $\in [96, 104]$, since $\xi(100) = 8$ without being perceived by the HVS. For a given EOTF, there is then a target range of luma code values that are best suited to embed a watermark in the spatial domain without being perceived by the HVS. We denote this target range by $luma_{target}$.

B. EMBEDDING REGION SELECTION

To guarantee that the embedded watermark in the spatial domain is imperceptible to the HVS, the ER must be uniform with luma codes $\in$ $luma_{target}$. Our approach to finding an ER that fulfils these criteria on the Y-channel is embodied in Algorithm 1.

In line 2 of Algorithm 1, function `superpixelSeg` is used to perform SLIC superpixel segmentation [28] on the Y-channel, which results in set $\mathcal{SP}$ with η superpixels (*SP*s). Superpixel segmentation divides the Y-channel into η homogeneous regions in terms of texture, color and visual semantics, which is a desirable property for watermarking [29]. In lines 4-5, the average luma code ($luma_{SP_k}$) and area ($area_{SP_k}$) of the k^{th} $SP \in \mathcal{SP}$ are computed, where $luma_{code}[p]$ is the p^{th} luma code and P is the total number of pixels in the k^{th} SP. In line 8, $luma_{SP_k}$ is normalized to [0,1], where 0 denotes the largest value in set SP and 1 the

Algorithm 1 ER Selection

Input: Y-channel
Output: ER

1: $\mathcal{SP} = \emptyset$; $\mathcal{SP}_{GS} = \emptyset$
2: $\mathcal{SP} = \{SP_1, SP_2, \cdots, SP_\eta\} \leftarrow$ `superpixelSeg`(Y)
3: **for each** $SP \in \mathcal{SP}$ **do**
4: $\quad luma_{SP_k} = \frac{1}{P}\sum_{p=1}^{P} luma_{code}[p]$
5: $\quad area_{SP_k} = P$
6: **end**
7: **for each** $SP \in \mathcal{SP}$ **do**
8: $\quad \widehat{luma}_{SP_k} \leftarrow$ `normalize`$(luma_{SP_k})$
9: $\quad \widehat{area}_{SP_k} \leftarrow$ `normalize`$(area_{SP_k})$
10: $\quad GS_{SP_k} = w_l \cdot \widehat{luma}_{SP_k} + w_a \cdot \widehat{area}_{SP_k}$
11: $\quad \mathcal{SP}_{GS} \leftarrow \mathcal{SP}_{GS} \cup GS_{SP_k}$
12: **end**
13: $\mathcal{SP}_{GS} \leftarrow$ `rank`$(\mathcal{SP}_{GS})$
14: $ER \leftarrow$ `inscribe`(SP_{GS_1})

smallest value in the set. In line 9, $area_{SP_k}$ is normalized to [0,1], where 0 denotes the smallest value in set SP and 1 the largest value in the set. In line 10, a global score, GS_{SP_k}, is computed for the k^{th} SP as a weighted average of $\widehat{luma}_{SP_k}$ and $\widehat{area}_{SP_k}$, with weights w_l and w_a, where $w_l > w_a$ and $w_l + w_a = 1$. In other words, GS_{SP_k} assigns higher importance to $\widehat{luma}_{SP_k}$, i.e., *SP*s with small luma code values are preferred over those with large areas (and possibly relatively large luma code values) to guarantee imperceptibility. In line 11, the GS_{SP_k} value is placed in set $\mathcal{SP}_{GS}$. In line 13, function `rank` organizes the elements in $\mathcal{SP}_{GS}$ in descending order, where the first element, $\mathcal{SP}_{GS_1}$, is the largest SP with the smallest $\widehat{luma}_{SP_k}$ value. Finally, in line 14, the ER is defined as the largest inscribed region within $\mathcal{SP}_{GS_1}$ by means of function `inscribe`. Fig. 10 (rows 1-3) shows sample results of Algorithm 1 on the Y-channel of various HDR images.

C. WATERMARK EMBEDDING

The HDR-IW method embeds a binary watermark, BW, of size $m \times n$ into the ER of size $m \times n$ to produce a watermarked ER denoted by $\overline{ER}$:

$$\overline{ER}_{i,j} = \begin{cases} ER_{i,j} + \Xi_{HDR} & \text{if } BW_{i,j} = 0 \\ ER_{i,j}, & \text{otherwise,} \end{cases} \tag{5}$$

where $\overline{ER}_{i,j}$ and $BW_{i,j}$ are the value of the watermarked ER and the binary watermark at pixel location (i, j), respectively, and Ξ_{HDR} is the embedding factor of the cover image. It is important to mention that the human visual attention and the HVS' response to contrast variations not only depend on the target region but also on its surrounding region [23], [24]. For this reason, the HDR-IW method accounts for the $\mathcal{L}_d$ values of the region surrounding the ER when embedding the watermark. The embedding factor of the cover image, Ξ_{HDR}, is then computed as a weighted sum of the average luma variation threshold of the ER, denoted by $\bar{\xi}_{ER}$; the average luma variation threshold of the region surrounding the ER,

FIGURE 10. (1st row) Superpixel segmentation on the Y-channel of various sample HDR images. (2nd row) Corresponding target superpixel. (3rd row) ER used to embed the watermark. (4th row) Watermarked images after adding the color channels in 4:2:0 YUV format.

denoted by $\bar{\xi}_{SR}$; and the average luma variation threshold of the cover image, denoted by $\bar{\xi}_{HDR}$:

$$\Xi_{HDR} = \lceil w_0 \cdot \bar{\xi}_{ER} + w_1 \cdot \left(\bar{\xi}_{SR} + \bar{\xi}_{HDR}\right) - k \rceil, \qquad (6)$$

where w_0 and w_1 are weights that establish the impact of the terms, with $w_0 + (2 \times w_1) = 1$, and k is a strength factor. The average luma variation thresholds in Eq. (6) are computed by averaging the luma variation thresholds of all the pixel locations in the corresponding region. For example, for the $m \times n$ ER, $\bar{\xi}_{ER}$ is computed as follows:

$$\bar{\xi}_{ER} = \frac{1}{m \cdot n} \sum_{i=1}^{m} \sum_{j=1}^{n} \xi_{i,j}(luma_{code}), \qquad (7)$$

where $\xi_{i,j}(luma_{code})$ is the luma variation threshold of pixel location (i, j) as given by the corresponding LVT curve (see Fig. 9). The region used to compute $\bar{\xi}_{SR}$ comprises the 8 blocks of size $m \times n$ surrounding the ER. To compute $\bar{\xi}_{HDR}$, all pixels locations of the cover image are used except for those in the ER and its surrounding region, as shown in Fig. 11.

Fig. 10 (4th row) shows sample watermarked images in the 4:2:0 YUV color format after embedding the binary watermark in Fig. 12 in the Y-channel. Fig. 13 graphically illustrates the complete embedding process.

D. DETECTION

A watermark embedded as explained in Section IV-C remains imperceptible to the HVS as long as the TF is not altered or the normal calibration and colorimetry conditions of the HDR screen remain unchanged. To make the watermark perceptible to the HVS, i.e., to visually detect it, one of the following procedures must be applied:

FIGURE 11. Regions used to compute the luma variation thresholds. ER is the $m \times n$ embedding region. SR comprises the eight $m \times n$ blocks surrounding ER. HDR comprises all pixels locations except for those in ER and SR.

FIGURE 12. Binary watermark used in this work.

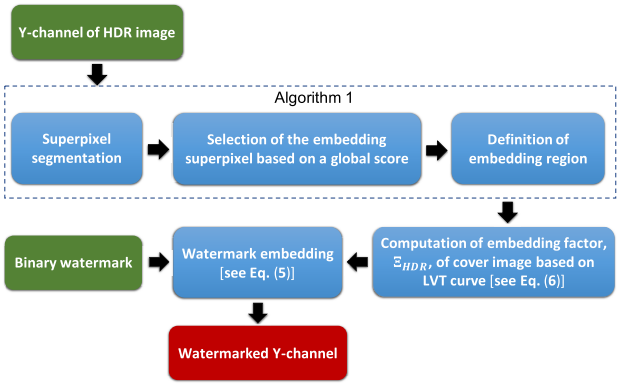

FIGURE 13. Block diagram of the embedding process. Blocks in green, red and blue denote inputs, outputs and processes, respectively.

1) Manual color calibration of the HDR screen. The EOTF, peak RGB gamut, luminance, black/white points, and greyscale settings of the HDR screen affect the screen's colorimetry. Therefore, manually modifying the HDR screen's colorimetry to display a brighter version of the watermarked HDR imaging highlights mid and bright tones, which enhances the current contrast. This contrast enhancement contributes to exaggerating the watermarked luma codes, thus making the watermark perceptible to the HVS. This is illustrated in Fig. 14 for the watermarked HDR images in Fig. 10 (4^{th} row).
2) Applying a gamma TF to the tone-mapped version of the watermarked HDR image. This process consists in varying the gamma factor of the traditional gamma TF, which is typically set to $\gamma = 2.2$. Applying a lower γ factor produces a brighter version of the tone-mapped image, thus making the watermark visible to the HVS.
3) Printing out the watermarked HDR image. The EOTF used by most printers is the dot gain compensation curve (DGCC), which is a variant of the traditional gamma function used by SDR screens [30]. The DGCC corresponds to luminance being reproduced as a power function of a code, where the exponent value is set to 1.75, instead of the traditional 2.2 value used for displaying purposes. Printing the watermarked HDR image involves applying a TMO,which is similar to the second procedure.
4) Using special software to handle color grading. Color grading aims to enhance the color of visual content by applying color correction and artistic color effects. Specialized color grading software performs a TMO and color correction with the traditional gamma TF, where γ can be modified to make the watermark perceptible to the HVS. This procedure is analogous to procedures 2 and 3.

V. EVALUATION RESULTS

Five sets of experiments are conducted to evaluate the proposed watermarking method to embed imperceptible binary watermarks in the spatial domain. These experiments evaluate the method's embedding payload, imperceptibility, and robustness. A total of 51 HDR images are used for evaluation. These HDR images are frames from a large collection of real-life HDR video sequences captured in a wide variety of scenarios and lighting conditions, including indoor and outdoor scenes, natural scenes, sports scenes, urban scenes, daytime scenes, night scenes, and textured scenes. Each HDR image has a resolution of 1920×1080 and is coded using Rec.2020 + PQ EOTF^{-1} or Rec.2020 + HLG OETF, as tabulated in the first four columns of Table 2 and illustrated in Fig. 15. The binary watermark in Fig. 12 is embedded in each test HDR image in all experiments.

In all evaluations, the weights to compute GS_{SP_k} in Algorithm 1 are set to $w_l = 0.6$ and $w_a = 0.4$. The weights to compute Ξ_{HDR} in Eq. (6) are set to $w_0 = 0.6$, $w_1 = 0.2$. Based on our evaluations, these values provide the strongest HVS-imperceptibility capabilities. This is confirmed in Figs. 16 and 17, which show the relationship between w_l and w_0, respectively, and the imperceptibility of a watermark embedded in image *ShowGirl2TeaserClip4000_25_12_P3ct2020_444i_300* [31], as tabulated in Table 2. We quantitatively measure the imperceptibility of the embedded watermark in terms of the HDR Visual Difference Predictor (HDR-VDP-2) [37]. This metric measures the visibility and quality of a pair of HDR images. The visibility describes the probability that an observer can distinguish differences between the two images and the quality measures the degradation that the original image suffers after watermarking. Both parameters are given in terms of an $u \times v$ probability map, $p(u, v) \in [0, 1]$, which is reduced to a single term by means of the Minkowsky distance:

$$\text{HDR-VDP-2} = \left(\sum_u \sum_v p(u, v)^\beta \right)^{1/\beta}, \tag{8}$$

where $\beta = 2.4$ is an adjusting factor, and u and v are coordinates for the current pixel location. To compare HDR-VDP-2 values with conventional metrics, Eq. (8) is converted to a dB scale [37]:

$$\text{HDR-VDP-2}_{\text{dB}} = 20 \cdot \log_{10} \left(\frac{\text{HDR-VDP-2}_{max}}{\text{HDR-VDP-2}} \right). \tag{9}$$

From Fig. 16, we can see that the imperceptibility is strongly affected for $w_l < 0.6$. Hence, to guarantee that an ER with the smallest luma code values is selected over others with large areas (and possibly relatively large luma code values), we use $w_l = 0.6$ and $w_a = 0.4$. From Fig. 17, we can see that values $w_0 < 0.6$ also decrease the imperceptibility. Therefore, we set $w_0 = 0.6$ and $w_1 = 0.2$.

A. FIRST SET OF EXPERIMENTS: EMBEDDING CAPACITY

Table 2 tabulates the size of the ER, in percentage w.r.t. the size of the cover image, the average luma code value of the ER, $\widehat{luma}_{ER}$, and the embedding factor of the cover image, Ξ_{HDR}. From this table, one can note that $\widehat{luma}_{ER}$ and Ξ_{HDR}

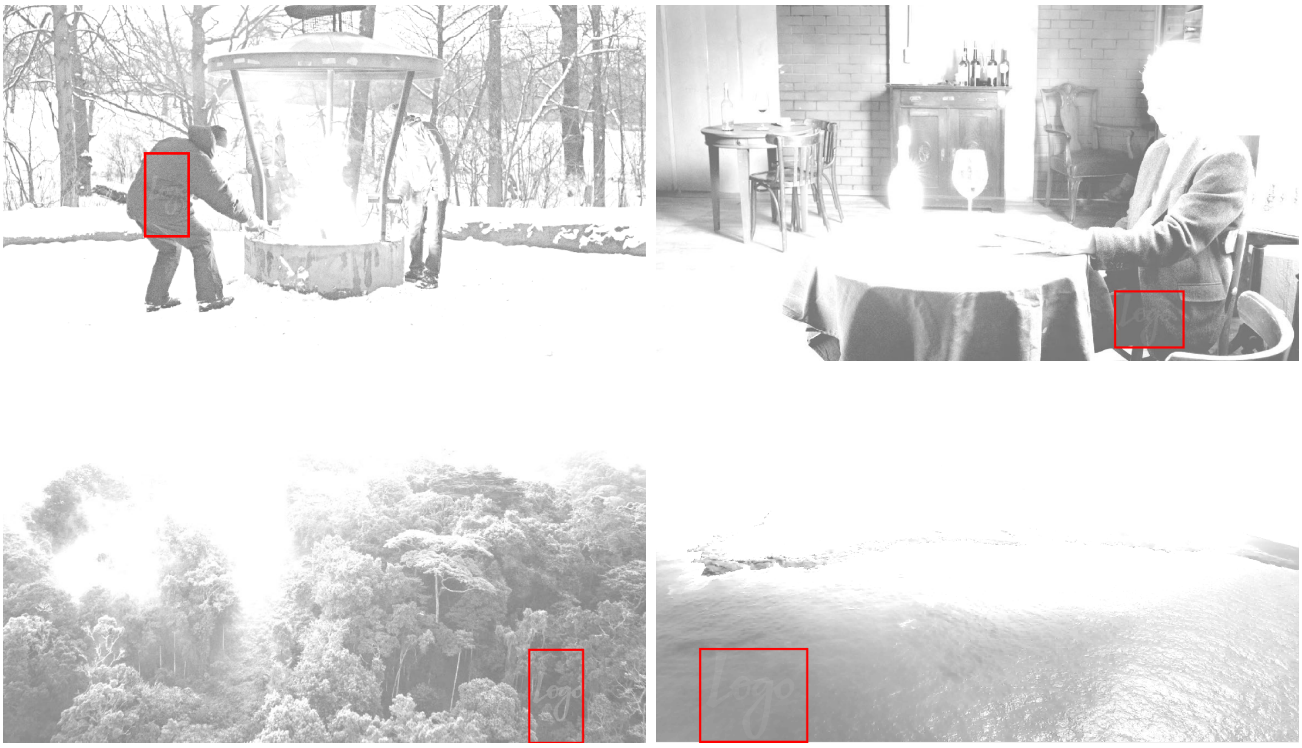

FIGURE 14. Watermarks (see Fig. 10) made visible after manual color calibration of the HDR screen.

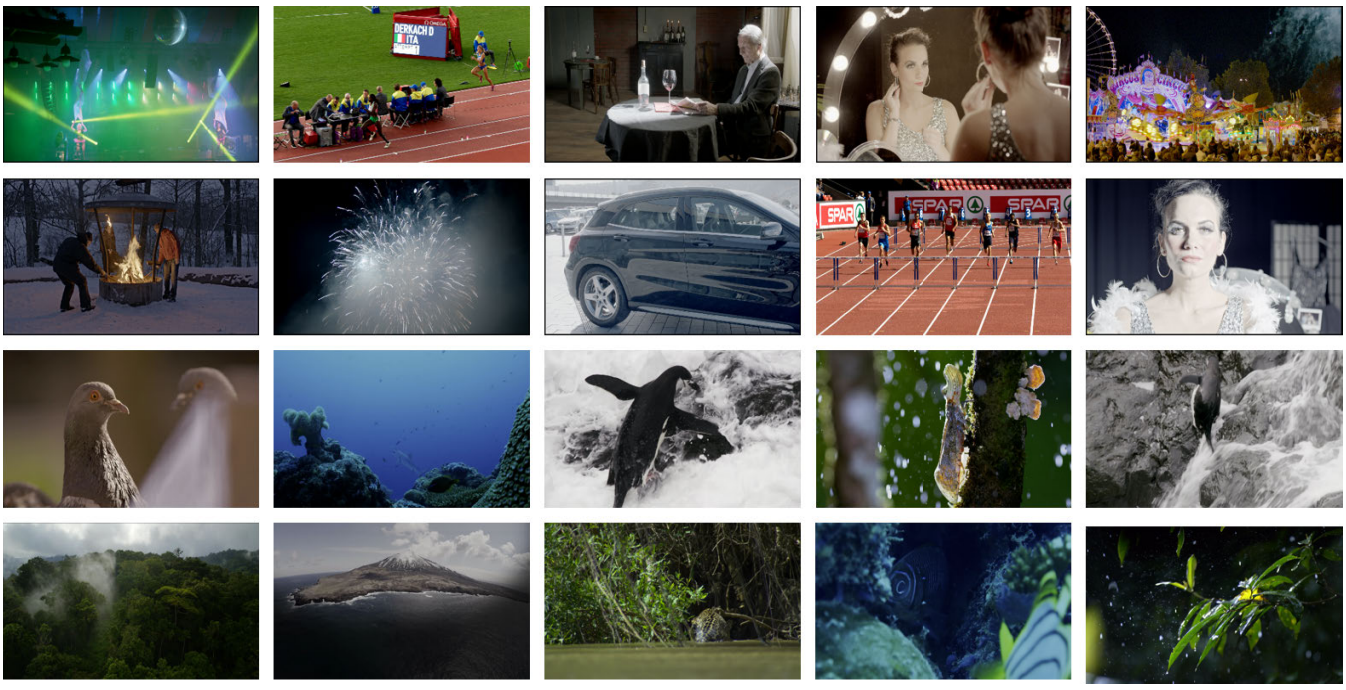

FIGURE 15. Sample test HDR images encoded using Rec.2020 + PQ EOTF^{-1} (rows 1-2) and Rec.2020 + HGL OETF (rows 3-4).

values depend on both, the image's content and the TF used. Namely, PQ-encoded images have positive Ξ_{HDR} values and lower $\widehat{luma}_{ER}$ values than HLG-encoded images, which have negative Ξ_{HDR} values. As shown in Fig. 1, the HLG TF uses a narrower range of codes than that used by the PQ TF to encode low luminance values. Therefore, low luminance regions of HGL-encoded images are then expected to have a larger average luma code value than that of PQ-encoded

TABLE 2. Performance evaluation of the HDR-IW method and two invisible HDR watermarking methods.

Source	Image name	ID	TF	ER_{size} (%)	$\widehat{luma}_{ER}$	Ξ_{HDR}	EC_{HDR}	Proposed method: HDR-IW		Method in [8]		Method in [9]	
								HDR-VDP-2	mPSNR	HDR-VDP-2	mPSNR	HDR-VDP-2	mPSNR
[31]	BeerFestTeaserClip4000_25_12_P3ct2020_444i_000	BF_000	PQ	7.26	65.0617	5	0.0549	47.5145	44.0568	43.0318	35.4686	37.2813	34.9757
	BeerFestTeaserClip4000_25_12_P3ct2020_444i_080	BF_080	PQ	0.57	64.4399	5	0.0415	45.8169	56.9533	44.0156	34.1435	35.8215	33.5727
	BeerFestTeaserClip4000_25_12_P3ct2020_444i_160	BF_160	PQ	0.44	64.2936	5	0.0413	53.5611	58.5206	44.7339	35.1188	35.6443	34.5371
	BeerFestTeaserClip4000_25_12_P3ct2020_444i_240	BF_240	PQ	0.44	64.8045	4	0.0372	41.5577	58.6405	42.0038	35.1347	35.8567	34.5676
	BeerFestTeaserClip4000_25_12_P3ct2020_444i_320	BF_320	PQ	0.89	86.2572	15	0.0826	41.4588	51.9660	45.9726	34.1767	40.5611	33.5904
	FireplaceTeaserClip4000_24_12_P3ct2020_444i_000	FP_000	PQ	0.79	95.4833	6	0.0460	44.9442	56.6304	41.4614	34.2924	32.7942	33.6542
	FireplaceTeaserClip4000_24_12_P3ct2020_444i_090	FP_090	PQ	0.52	93.9832	14	0.0778	41.9927	54.9763	39.8397	34.3107	33.3617	33.6748
	FireplaceTeaserClip4000_24_12_P3ct2020_444i_170	FP_170	PQ	5.71	87.7632	7	0.0599	49.6649	47.2802	40.1855	34.0890	38.6916	33.4235
	FireplaceTeaserClip4000_24_12_P3ct2020_444i_230	FP_230	PQ	5.19	87.3795	5	0.0508	49.8233	48.6361	43.4615	33.8603	36.0432	33.1753
	ShowGirl2TeaserClip4000_25_12_P3ct2020_444i_000	SG_000	PQ	6.64	66.5731	5	0.0537	50.3415	46.5019	41.9311	33.6824	31.7275	33.0048
	ShowGirl2TeaserClip4000_25_12_P3ct2020_444i_134	SG_134	PQ	8.88	64.7842	5	0.0582	48.2245	45.1176	42.4254	33.6269	32.4126	32.9472
	ShowGirl2TeaserClip4000_25_12_P3ct2020_444i_154	SG_154	PQ	8.88	64.7048	5	0.0582	48.9187	43.1384	40.1463	34.3596	31.6520	33.7397
	ShowGirl2TeaserClip4000_25_12_P3ct2020_444i_240	SG_240	PQ	8.83	88.1832	9	0.0581	44.0628	57.8471	40.1115	32.8159	38.7048	32.0597
	ShowGirl2TeaserClip4000_25_12_P3ct2020_444i_300	SG_300	PQ	2.17	87.0180	5	0.0447	45.5536	55.7334	41.7723	33.1254	36.5800	32.4266
	ShowGirl2TeaserClip4000_25_12_P3ct2020_444i_338	SG_338	PQ	5.19	85.6985	9	0.0508	50.8921	55.8079	40.9829	33.2976	37.0838	32.6051
[32]	beerfest_lightshow_102844	bf_2844	PQ	0.31	69.0381	15	0.0758	53.3829	61.3531	44.0004	33.805	33.9029	33.2215
	beerfest_lightshow_103020	bf_3020	PQ	0.20	69.0659	13	0.0820	45.3588	63.4394	39.6001	33.0551	42.5977	32.5231
	beerfest_lightshow_103660	bf_3660	PQ	0.89	68.4265	15	0.0818	43.9821	56.5541	32.4812	33.0182	37.3207	32.3887
	bistro_090958	b_0958	PQ	1.23	70.0706	14	0.0865	41.4252	51.4648	38.1366	34.4452	37.1528	33.7897
	bistro_091470	b_1470	PQ	2.59	120.868	10	0.0941	45.4038	55.6251	33.5132	32.3698	37.2952	32.6893
	bistro_091710	b_1710	PQ	3.05	69.7418	14	0.0958	41.7908	50.5472	39.5097	33.4386	37.8302	32.7635
	bistro_091780	b_1780	PQ	1.23	72.7077	5	0.0857	44.4863	53.8816	40.1473	33.4500	39.361	32.7253
	carousel_fireworks_096184	cf_6184	PQ	3.09	79.6111	4	0.0967	42.2710	50.4985	38.5956	33.1583	31.1773	32.4579
	carousel_fireworks_096270	cf_6270	PQ	9.00	70.0666	5	0.1384	47.3657	43.4386	44.1722	34.3907	40.3130	33.7857
	carousel_fireworks_096640	cf_6640	PQ	8.96	64.0895	5	0.1359	46.7792	43.0837	35.1474	34.5604	40.2895	34.0380
	carousel_fireworks_097400	cf_7400	PQ	5.75	64.2982	5	0.0955	44.2614	46.9478	43.8492	33.0736	35.9975	32.4252
	cars_fullshot_132340	cfs_2340	PQ	0.44	92.9170	15	0.0801	52.9946	55.0406	46.3237	33.1294	32.5863	32.4803
	hdr_testimage_273335	hdr_3335	PQ	0.20	151.018	10	0.0699	52.6005	66.5421	44.9146	34.1050	36.6963	33.4715
	poker_fullshot_045787	pf_5787	PQ	0.41	74.0759	15	0.0921	53.6566	54.6822	45.0648	34.0513	32.9704	33.3800
	pokertravelling_slowmotion_033122	ps_3122	PQ	3.19	64.2887	6	0.0872	49.0392	50.2825	47.9129	33.8515	39.2887	33.1749
	showgirl_01_235636	sg_5636	PQ	0.69	64.2887	15	0.0668	57.0186	51.9075	38.2519	33.0537	33.4718	32.2670
	showgirl_01_235965	sg_5965	PQ	1.93	74.4185	15	0.0677	42.4738	49.5097	41.9896	33.3425	35.0797	32.6219
	smith_hammering_252764	sh_2764	PQ	5.12	102.222	15	0.1339	47.6781	55.1725	41.6906	34.948	32.7324	34.4605
[33]	EBU_ZurichAthletics2014HD100p_HDREXR_04272	EBU_4272	PQ	0.73	64.1212	15	0.0815	44.3670	53.3337	44.2540	38.2483	42.4166	34.9571
	EBU_ZurichAthletics2014HD100p_HDREXR_06998	EBU_6998	PQ	0.13	64.5464	15	0.0754	57.5099	60.8063	45.8793	37.2843	41.5918	34.3373
	Average over PQ-encoded images (PQ AV)				**74.0591**	**8.66**	**0.0751**	**47.6857**	**55.2008**	**41.6431**	**34.0652**	**36.4082**	**33.3118**
[34]	BBC_1_bbc_HLG_s012	bbc1_012	HLG	3.36	105.9323	-10	0.1501	48.7965	56.1623	44.3152	33.8072	39.8490	33.8041
	BBC_1_bbc_HLG_s036	bbc1_036	HLG	0.37	165.2959	-10	0.1471	51.4153	67.9249	43.1472	33.1944	39.9151	33.1909
	BBC_1_bbc_HLG_s306	bbc1_306	HLG	2.09	117.8460	-11	0.1390	52.8173	55.9453	44.4887	33.7585	44.4815	33.7569
	BBC_1_bbc_HLG_s320	bbc1_320	HLG	1.10	76.8822	-10	0.1478	53.8029	57.9253	47.5049	37.5390	45.7309	32.5366
	BBC_1_bbc_HLG_s435	bbc1_435	HLG	0.59	85.8327	-10	0.1473	57.3028	61.0855	47.8086	38.2134	47.1820	33.2112
	BBC_1_bbc_HLG_s598	bbc1_598	HLG	0.36	142.1681	-15	0.0982	64.2180	65.2878	49.8506	37.1877	45.4032	32.1842
	BBC_1_bbc_HLG_s601	bbc1_601	HLG	0.60	93.2377	-20	0.0495	67.2617	53.3055	44.4728	38.4868	43.3119	33.4840
[35]	BBC_C1_bbcc1_HLG_s005	bbcc1_s005	HLG	1.25	95.6598	-18	0.0697	50.6502	52.3055	48.4916	33.1920	40.3850	33.1895
	BBC_C1_bbcc1_HLG_s014	bbcc1_014	HLG	2.89	83.7985	-20	0.0518	51.5319	47.2546	48.5842	34.4151	48.4451	34.4153
	BBC_C1_bbcc1_HLG_s048	bbcc1_048	HLG	0.59	99.6077	-18	0.0691	54.5520	52.9652	51.4338	35.1299	38.3687	34.1285
	BBC_C1_bbcc1_HLG_s066	bbcc1_066	HLG	0.97	108.8368	-20	0.0499	51.4165	55.3831	50.6727	38.4945	40.0680	33.4914
[36]	BBC_C2_bbcc2_HLG_018	bbcc2_s018	HLG	3.33	99.1747	-20	0.0522	55.8084	47.8356	55.3290	39.6010	48.3933	34.6056
	BBC_C2_bbcc2_HLG_s031	bbcc2_031	HLG	3.16	87.8270	-20	0.0521	47.8915	47.3141	47.8720	34.9953	46.8846	34.9976
	BBC_C2_bbcc2_HLG_s045	bbcc2_045	HLG	1.62	91.4447	-18	0.0701	53.6596	51.7501	49.2053	46.7563	45.2401	34.7593
	BBC_C2_bbcc2_HLG_s092	bbcc2_092	HLG	0.37	102.2924	-18	0.0688	56.6664	56.5711	45.4685	37.5548	43.1919	33.5531
	BBC_C2_bbcc2_HLG_s095	bbcc2_095	HLG	0.74	104.4708	-15	0.0986	52.7796	56.7392	45.0768	37.7707	42.9350	34.7696
	Average over HGL-encoded images (HLG AV)				**103.6442**	**-15.81**	**0.0913**	**54.4107**	**55.3708**	**47.7326**	**36.8810**	**43.7366**	**33.7549**
	Average over all images (OAV)							**51.0482**	**55.2858**	**44.6879**	**35.4731**	**40.0724**	**33.5333**

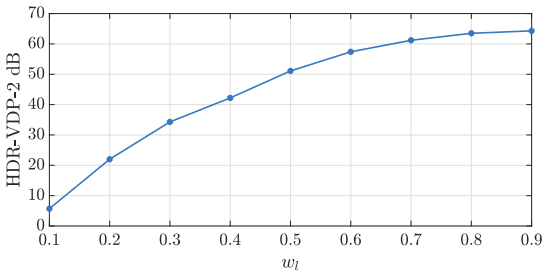

FIGURE 16. Imperceptibility (HDR-VDP-2 dB) of a watermark embedded in the ER selected by Algorithm 1 for different w_l values.

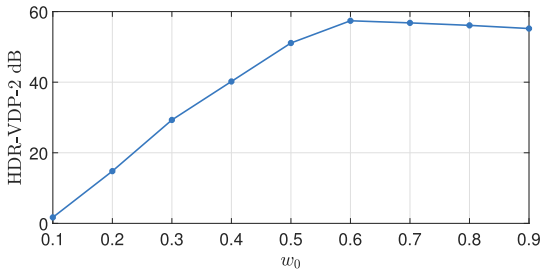

FIGURE 17. Imperceptibility (HDR-VDP-2 dB) of a watermark embedded in the ER using an embedding factor computed by Eq. (6) for different w_0 values.

images. To embed imperceptible watermarks in the spatial domain of HLG-encoded images, the Ξ_{HDR} value should be then negative, otherwise, the embedded information may be perceived by the HVS as medium tones. On the other hand, to embed imperceptible watermarks in the spatial domain of PQ-encoded images, the Ξ_{HDR} value should be positive. Based on our evaluations on the test images, such Ξ_{HDR} values are achieved by setting the strength factor, k, to $\{5, 25\}$ for PQ-encoded and HLG-encoded images, respectively [see Eq. (6)]. Additionally, as shown in Table 2, absolute Ξ_{HDR} values of HLG-encoded images tend to be larger than those of PQ-encoded images. The HLG TF has a relatively low granularity of luma codes for low luminance values. Consequently, there is more room to modify these codes aggressively before the changes can be perceived by the HVS. This particular TF uses large coding steps in low luminance regions to code large luminance variations. Consequently, if a luma code is modified by a value $< \Xi_{HDR}$, the HVS may not be able to perceive the embedded watermark even after the TF is altered or the normal calibration and colorimetry conditions of the HDR screen are changed. This is because the ER's watermarked luma codes may still be within the range of values of the surrounding region. On the other hand, the PQ TF has a high granularity of luma codes for low luminance

values. Therefore, modifying these codes aggressively increases the risk that the HVS can perceive the changes.

Based on the previous discussions, one can conclude that, in general, HLG-coded images allow for larger imperceptible variations to low-valued luma codes than PQ-encoded images. Such variations, however, can only be applied if the ER has luma codes $\in$ $luma_{target}$, i.e., the range of luma codes that are best suited to embed a watermark in the spatial domain that is imperceptible to the HVS.

Let us recall that the HDR-IW method combines the content readability afforded by invisible watermarking and the visual ownership identification afforded by visible watermarking. As with any other watermarking method in the spatial domain, determining the embedding payload is challenging, as watermarks may be embedded by altering the whole cover media or a small region of it. The embedding payload of a watermarking method in the spatial domain is then dependent on the content of the cover media and the level of distortion introduced by modifying pixel values. Since the HDR-IW method indeed combines aspects of visible watermarking and invisible watermarking, we propose a new metric to quantitatively compute its embedding payload. Our metric, EC_{HDR}, accounts for the contents of the cover media and the TF. Specifically, it accounts for the size of the ER and the $\bar{\xi}$ values:

$$EC_{HDR} = w_2 \cdot ER_{size} + w_3 \cdot \frac{w_0 \cdot \bar{\xi}_{ER} + w_1 \cdot \left(\bar{\xi}_{SR} + \bar{\xi}_{HDR}\right)}{\max\left(\xi[luma_{target}]\right)} \in [0, 1], \tag{10}$$

where $ER_{size} \in [0, 1]$, $\max\left(\xi[luma_{target}]\right)$ is the maximum $\xi(luma_{code})$ value for the range $luma_{target}$ (see Fig. 9), $\{w_0, w_1\}$ are weights as defined before [see Eq. (6)], and $\{w_2, w_3\}$ are weights that establish the importance of each constituent term of the EC_{HDR} metric, with $w_2 + w_3 = 1$. A value $EC_{HDR} = 1$ denotes the highest embedding payload, e.g., when the ER spans the entire cover image and the second term of Eq. (10) $= 1$.

Column 8 of Table 2 tabulates EC_{HDR} values for the test images with $\{w_2 = 0.2, w_3 = 0.8\}$, i.e., by giving more importance to the second term as ER regions are, in general, relatively small and unlikely to span the entire cover image. Note that the EC_{HDR} metric indeed accounts for the cover's content and the TF used. For example, image BF_100 has an embedding payload $EC_{HDR} = 0.0549$, which is less than the embedding payload of image BF_320 ($EC_{HDR} = 0.0826$), despite the fact that image BF_100 has a larger ER than that of image BF_320. Image BF_100 has, however, a lower Ξ_{HDR} value, hence, the embedding payload is expected to be relatively small. As expected, HLG-coded images have the largest embedding payloads with a maximum value of $EC_{HDR} = 0.1501$ for the test images.

B. SECOND SET OF EXPERIMENTS: IMPERCEPTIBILITY

Let us recall that the HDR-IW method operates in the spatial domain by modifying pixels values in the Y-channel. It is then expected that the visual quality, both quantitative and qualitative, of the cover media is disrupted. However, since the embedded watermarks cannot be perceived by the HVS, these disruptions are expected to be non-existent or minimal. To confirm that the embedded watermarks are imperceptible to the HVS, we use two quantitative metrics that measure imperceptibility: the HDR-VDP-2 metric and the multi-exposure Peak Signal to Noise Ratio (mPSNR) [38].

The mPSNR measures the error in a watermarked HDR image by first computing a series of exposure levels, which are tone-mapped by a gamma curve after exposure compensation. The tone-mapped version of an HDR image, I, is given by:

$$T(I, e) = \left[255 \cdot \left(2^e \cdot I\right)^{1/\gamma}\right]_0^{255}, \tag{11}$$

where e is the current f-stop, which represents a variation in the aperture of a camera, $\gamma = 2.2$, and $[\cdot]_0^{255}$ indicates clamping to the integer interval [0, 255]. The mPSNR is then computed by using the mean square error (MSE) over a total of E exposure levels:

$$mPSNR = 10 \cdot \log_{10}\left(\frac{3 \cdot 255^2}{MSE}\right), \tag{12}$$

$$MSE = \frac{1}{E \cdot W \cdot H} \sum_E \sum_{x,y} \left(\Delta R_{xy}^2 + \Delta G_{xy}^2 + \Delta B_{xy}^2\right), \tag{13}$$

where $\{W, H\}$ are the width and height of I, respectively, and $\{\Delta R_{xy}, \Delta G_{xy}, \Delta B_{xy}\}$ are the errors in the R, G, and B components, respectively. For an f-stop, e, these errors are computed after computing $T(I, e) - T(\tilde{I}, e)$, where $\tilde{I}$ is the watermarked image [38].

To the best of our knowledge, no watermarking method for HDR imaging in the spatial domain with HVS-imperceptibility capabilities has been previously proposed. However, in this second set of experiments, we also evaluate the invisible watermarking methods in [8], [9], which are proposed for HDR images and operate in the frequency domain by applying the DWT.

HDR-VDP-2 and mPSNR values are tabulated in the last six columns of Table 2. For the HDR-IW method, images with large ERs, i.e., $ER_{size} > 2.5\%$, tend to have the lowest HDR-VDR-2 values. Note also that PQ-encoded images tend to be more robust to degradations introduced by watermarking, as HDR-VDR-2 values for these images are, on average, higher than those of HGL-encoded images. mPSNR values do not tend to significantly vary according to the TF or the ER size for the HDR-IW method. For the majority of the test HDR images, both metrics are within an acceptable range, which confirms that the HDR-IW method can indeed embed watermarks in the spatial domain that are imperceptible to the HVS.

TABLE 3. Qualitatively evaluation of the HDR-IW method in terms of the MOS: percentage of watermarked HDR images assigned to each of the four scores.

Source	TF	Score 1	Score 2	Score 3	Score 4	Disturbing (%)
[31]	PQ	0	0	4.89	95.11	5.55
[32]	PQ	0	0	5.18	94.81	5.55
[33]	PQ	0	0	0	100	0
PQ AV		**0**	**0**	**3.35**	**96.64**	**3.70**
[34]	HLG	0	0	3.81	96.19	6.66
[35]	HLG	0	0	1.66	98.33	2.25
[36]	HLG	0	0	0	100	0
HLG AV		**0**	**0**	**1.82**	**98.17**	**2.97**
OAV		**0**	**0**	**2.59**	**97.40**	**3.33**

TABLE 4. Qualitatively evaluation of method in [8] in terms of the MOS: percentage of watermarked HDR images assigned to each of the four scores.

Source	TF	Score 1	Score 2	Score 3	Score 4	Disturbing (%)
[31]	PQ	0	0	5.33	94.67	3.11
[32]	PQ	0	0	27.41	72.60	13.33
[33]	PQ	0	0	90	10	36.66
PQ AV		**0**	**0**	**40.91**	**59.09**	**17.70**
[34]	HLG	0	0	23.81	76.19 0	7.61
[35]	HLG	0	0	11.66	88.34	5.00
[36]	HLG	0	0	5.33	94.67	2.66
HLG AV		**0**	**0**	**13.6**	**86.40**	**5.09**
OAV		**0**	**0**	**27.25**	**72.74**	**11.39**

TABLE 5. Qualitatively evaluation of the method in [9] in terms of the MOS: percentage of watermarked HDR images assigned to each of the four scores.

Source	TF	Score 1	Score 2	Score 3	Score 4	Disturbing (%)
[31]	PQ	0	33.78	41.78	24.44	12.89
[32]	PQ	0	42.96	28.15	28.89	33.70
[33]	PQ	0	0	36.67	63.33	46.66
PQ AV		**0**	**25.58**	**35.53**	**38.88**	**31.08**
[34]	HLG	0	0	14.28	85.71	4.76
[35]	HLG	0	0	28.33	71.66	3.33
[36]	HLG	0	0	2.66	97.33	2.66
HLG AV		**0**	**0**	**15.09**	**84.9**	**3.58**
OAV		**0**	**12.79**	**25.31**	**61.89**	**17.33**

Overall, the HDR-IW method attains a higher imperceptibility, in terms of HDR-VDP-2 and mPSNR, than that of the methods in [8], [9]. The lower HDR-VDP-2 and mPSNR values attained by the methods in [8], [9] are due to the fact these methods do not account for the EOTFs needed to display HDR images on a screen.

To qualitatively measure the imperceptibility of the embedded watermarks, we use the Mean Opinion Score (MOS) as the metric. Specifically, fifteen observers with various experience levels in HDR imaging have visually inspected each watermarked image on a laptop built-in HDR screen of 17 inches wide with Windows 10 HDR advanced color settings enabled. The observers are asked to identify the watermark in a variety of lighting conditions and are given the opportunity to analyze the watermarked images from any distance and viewing angle. Results from this evaluation are collected using four scores ranging from 1 to 4, where 1 corresponds to full perceptibility and 4 to full imperceptibility. In cases where the observer is able to perceive the watermark (scores 1 - 3), the observer is asked to determine if the watermark is visually disturbing. The percentage of watermarked HDR images assigned to each of the four scores is tabulated in Tables 3 - 5 for the HDR-IW method and the methods in [8], [9], respectively.

Results in Tables 3 - 5 further confirm that the HDR-IW method can embed watermarks in the spatial domain that are imperceptible to the HVS. In the few cases where the watermark can be barely perceived (score 3), only a very small percentage of images is found to be visually disturbing. Note that the lower MOS values assigned to the images watermarked by the methods in [8], [9] also show the importance of accounting for the EOTF in the embedding process, as this TF is needed to display the HDR image on a screen. Hence, visual distortions may be introduced if this TF is not accounted for even if the watermark is embedded in the frequency domain.

It is worth further emphasizing the importance of the LVT curve in the computation of the luma variation threshold (ξ) and the embedding factor (Ξ_{HDR}) to guarantee both imperceptibility and detection of the watermark in the HDR-IW method. For instance, in Fig. 18, the binary watermark is embedded using an arbitrary embedding factor which leads to full perceptibility, even when the watermark is embedded in the ER selected by Algorithm 1. Similarly, if the binary watermark is embedded in a region different from the ER selected by Algorithm 1, but using the Ξ_{HDR} for the appropriate ER, the watermark is also fully perceptible, as shown in Fig. 19.

FIGURE 18. Watermarked HDR imaging using an arbitrary embedding factor, Ξ_{HDR}.

FIGURE 19. Wartermarked HDR imaging using an arbitrary ER.

TABLE 6. Percentage of watermarked HDR images assigned a Score = 4 (MOS) after applying a TMO using several watermarking methods.

Source	TF	TMOs on the proposed HDR-IW method					TMOs on the method in [8]					TMOs on the method in [9]				
		C-TM	G-TM	H-TM	M-TM	R-TM	C-TM	G-TM	H-TM	M-TM	R-TM	C-TM	G-TM	H-TM	M-TM	R-TM
[31]	PQ	93.33	85	90	91.66	90	54.22	87.11	82.66	80	76.00	45.33	46.66	51.55	51.11	52.44
[32]	PQ	94.44	98.61	94.44	98.61	97.22	58.51	70.90	59.39	69.09	61.818	29.62	25.92	29.25	36.66	41.85
[33]	PQ	100	100	100	100	100	0	0	0	0	0	6.66	10	3.33	6.66	6.66
PQ AV		**95.92**	**94.53**	**94.81**	**96.75**	**95.74**	**37.58**	**52.67**	**47.35**	**49.69**	**45.93**	**27.20**	**27.53**	**28.04**	**31.48**	**33.65**
[34]	HLG	96.42	96.42	100	96.42	92.85	39.04	50.47	50.47	52.38	40.95	50.47	84.76	72.38	71.42	67.61
[35]	HLG	93.75	100	100	100	100	86.66	92.33	88.33	58.33	86.66	91.66	95	93.33	88.33	90
[36]	HLG	100	100	100	100	95	70.66	78.66	77.33	76	81.33	96	98.66	94.66	89.33	93.33
HLG AV		**96.72**	**98.80**	**100**	**98.80**	**95.95**	**65.46**	**73.82**	**72.04**	**62.23**	**69.65**	**79.38**	**92.80**	**86.79**	**83.03**	**83.65**
OAV		**96.32**	**96.67**	**97.40**	**97.78**	**95.84**	**51.52**	**63.24**	**59.70**	**55.96**	**957.79**	**53.29**	**60.17**	**57.42**	**57.25**	**58.65**

TABLE 7. BER values of the extracted binary watermarks after applying various TMOs.

Source	ID	TF	TMOs on the proposed HDR-IW method					TMOs on the method in [8]					TMOs on the method in [9]				
			C-TM	G-TM	H-TM	M-TM	R-TM	C-TM	G-TM	H-TM	M-TM	R-TM	C-TM	G-TM	H-TM	M-TM	R-TM
[31]	BF_000	PQ	0.0236	0.0246	0.0150	0.2066	0.0236	0.2071	0.2072	0.2068	0.2067	0.2073	0.5034	0.5071	0.5527	0.5035	0.4978
	FP_230	PQ	0.0976	0.1011	0.0487	0.0976	0.1031	0.2072	0.2073	0.2067	0.2072	0.2073	0.4426	0.4735	0.4769	0.4446	0.4484
	SG_134	PQ	0.0260	0.0273	0.0126	0.0260	0.0278	0.2072	0.2073	0.2068	0.2072	0.2073	0.4769	0.5052	0.5004	0.4852	0.4834
	SG_154	PQ	0.0327	0.0335	0.0186	0.0327	0.0343	0.2071	0.2072	0.2069	0.2071	0.2072	0.5068	0.5245	0.5507	0.5123	0.5095
[32]	bf_3660	PQ	0.0866	0.0875	0.0709	0.0866	0.0884	0.2076	0.2075	0.2072	0.2066	0.2075	0.4519	0.4955	0.4593	0.4605	0.4633
	cf_6640	PQ	0.0031	0.0031	0.0030	0.0046	0.0049	0.2070	0.2071	0.2070	0.2070	0.2070	0.5496	0.5451	0.6079	0.5518	0.5436
	cf_7400	PQ	0.0034	0.0549	0.0032	0.0530	0.0034	0.2067	0.2067	0.2066	0.2067	0.2067	0.4566	0.4894	0.4831	0.4628	0.4640
	hdr_3335	PQ	0.1184	0.1060	0.1155	0.1184	0.1381	0.2070	0.2072	0.2068	0.2071	0.2073	0.4624	0.4586	0.4561	0.4572	0.4503
	sg_5636	PQ	0.0244	0.0247	0.0286	0.0244	0.0441	0.2072	0.2073	0.2069	0.2070	0.2072	0.5007	0.4660	0.4776	0.4973	0.4931
[33]	EBU_4272	PQ	0.0060	0.0060	0.0054	0.0054	0.0061	0.6122	0.6030	0.6171	0.6109	0.6099	0.4473	0.5603	0.4717	0.4828	0.4975
PQ AV			**0.0327**	**0.0360**	**0.0245**	**0.0359**	**0.0365**	**0.2475**	**0.2467**	**0.2478**	**0.2474**	**0.2473**	**0.4798**	**0.5025**	**0.5036**	**0.4858**	**0.4851**
[34]	bbc1_012	HLG	0.1569	0.1490	0.2070	0.1569	0.1330	0.2549	0.2371	0.2854	0.2245	0.2141	0.2695	0.2660	0.2713	0.2653	0.2643
	bbc1_306	HLG	0.1203	0.1724	0.2417	0.1203	0.1740	0.4251	0.4559	0.5042	0.4245	0.4231	0.2831	0.2674	0.2692	0.2718	0.2716
	bbc1_435	HLG	0.0753	0.1853	0.0426	0.0753	0.1919	0.4058	0.3673	0.4460	0.3999	0.3851	0.2743	0.2593	0.2681	0.2687	0.2638
[35]	bbcc1_005	HLG	0.0703	0.0705	0.1237	0.0703	0.0708	0.5619	0.3065	0.3327	0.4497	0.4018	0.3202	0.3175	0.3063	0.2998	0.2976
	bbcc1_048	HLG	0.0756	0.0713	0.2421	0.0756	0.0682	0.3364	0.3256	0.4241	0.3328	0.3235	0.2803	0.2734	0.2928	0.2754	0.2792
	bbcc1_066	HLG	0.0903	0.0823	0.2007	0.0903	0.0804	0.2313	0.2402	0.3089	0.2314	0.2277	0.2611	0.2564	0.2560	0.2612	0.2544
[36]	bbcc2_031	HLG	0.0634	0.0627	0.1097	0.0634	0.0625	0.4642	0.4647	0.5921	0.4637	0.4565	0.2723	0.2738	0.2811	0.2720	0.2694
	bbcc2_045	HLG	0.1053	0.1013	0.1834	0.1053	0.1017	0.4707	0.4669	0.5960	0.4704	0.4622	0.2717	0.2719	0.2814	0.2717	0.2691
	bbcc2_092	HLG	0.0743	0.0750	0.0650	0.0743	0.0749	0.2552	0.2533	0.3740	0.2539	0.2468	0.2789	0.2778	0.2787	0.2760	0.2722
	bbcc2_095	HLG	0.1585	0.1587	0.1324	0.1585	0.1587	0.3292	0.3182	0.4528	0.3250	0.3183	0.2663	0.2672	0.2752	0.2654	0.2647
HLG AV			**0.0989**	**0.1143**	**0.1653**	**0.0989**	**0.1130**	**0.3735**	**0.3436**	**0.4316**	**0.3576**	**0.3459**	**0.2778**	**0.2731**	**0.2780**	**0.2727**	**0.2706**
OAV			**0.0658**	**0.0751**	**0.0949**	**0.0674**	**0.0747**	**0.3105**	**0.2951**	**0.3397**	**0.3025**	**0.2967**	**0.3788**	**0.3878**	**0.3908**	**0.3793**	**0.3779**

TABLE 8. BER values of the extracted binary watermarks after applying HEVC lossy compression.

Source	ID	TF	Proposed HDR-IW method				Method in [8]				Method in [9]			
			$QP = 0$	$QP = 10$	$QP = 20$	$QP = 40$	$QP = 0$	$QP = 10$	$QP = 20$	$QP = 40$	$QP = 0$	$QP = 10$	$QP = 20$	$QP = 40$
[31]	BF_000	PQ	0.0136	0.0186	0.0425	0.2043	0.2111	0.2107	0.2094	0.2114	0.3618	0.4113	0.6721	0.7244
	FP_230	PQ	0.0430	0.0440	0.0564	0.1768	0.2072	0.2071	0.2077	0.2093	0.3298	0.3493	0.5092	0.7068
	SG_134	PQ	0.0107	0.0132	0.0601	0.1993	0.2069	0.2041	0.2090	0.2087	0.3666	0.3877	0.5150	0.6680
	SG_154	PQ	0.0146	0.0181	0.0443	0.2051	0.2070	0.2071	0.2082	0.2090	0.3872	0.4037	0.5302	0.6817
[32]	bf_3660	PQ	0.0653	0.0748	0.1748	0.2386	0.2111	0.2107	0.2094	0.2114	0.3593	0.3871	0.5921	0.2975
	cf_6640	PQ	0.0003	0.0082	0.0406	0.1801	0.2072	0.2074	0.2093	0.2096	0.4786	0.4891	0.5584	0.3891
	cf_7400	PQ	0.0001	0.0048	0.0300	0.1750	0.2069	0.2071	0.2087	0.2109	0.3761	0.4078	0.6581	0.7208
	hdr_3335	PQ	0.1048	0.0999	0.0935	0.2443	0.2069	0.2071	0.2086	0.2094	0.3530	0.3795	0.6331	0.7246
	sg_5636	PQ	0.0222	0.0263	0.0671	0.2062	0.2076	0.2071	0.2077	0.2094	0.3842	0.4035	0.5281	0.3563
[33]	EBU_4272	PQ	0.0026	0.0129	0.0726	0.2118	0.6179	0.6221	0.6333	0.7236	0.3651	0.3899	0.3094	0.4852
PQ AV			**0.0205**	**0.0264**	**0.0682**	**0.2057**	**0.2485**	**0.2490**	**0.2506**	**0.2609**	**0.3762**	**0.4009**	**0.5506**	**0.5754**
[34]	bbc1_012	HLG	0.1135	0.1180	0.1026	0.2069	0.5062	0.2981	0.2579	0.2372	0.2972	0.3217	0.4282	0.4239
	bbc1_306	HLG	0.0716	0.0776	0.1116	0.2057	0.5031	0.3266	0.2749	0.2475	0.3010	0.3285	0.4199	0.4653
	bbc1_435	HLG	0.0347	0.0415	0.1420	0.2065	0.3993	0.2800	0.2558	0.2411	0.2687	0.2976	0.4243	0.4193
[35]	bbcc1_005	HLG	0.0585	0.0583	0.0807	0.1930	0.4985	0.4087	0.3026	0.2746	0.3070	0.3292	0.3948	0.4709
	bbcc1_048	HLG	0.0591	0.0610	0.1162	0.2060	0.4953	0.3136	0.2685	0.2475	0.2907	0.3104	0.4125	0.4209
	bbcc1_066	HLG	0.0526	0.0564	0.0709	0.2840	0.5389	0.2840	0.2478	0.2346	0.2774	0.2952	0.3958	0.3719
[36]	bbcc2_031	HLG	0.0513	0.0597	0.0694	0.1930	0.4637	0.3617	0.2977	0.2648	0.3147	0.3340	0.4036	0.4471
	bbcc2_045	HLG	0.0885	0.0925	0.1378	0.1988	0.5047	0.3718	0.3052	0.2688	0.3081	0.3287	0.3966	0.4431
	bbcc2_092	HLG	0.0533	0.0617	0.0810	0.2145	0.4788	0.3682	0.2927	0.2658	0.3088	0.3307	0.3977	0.4464
	bbcc2_095	HLG	0.1296	0.1359	0.1548	0.2049	0.5063	0.3451	0.2821	0.2591	0.3026	0.3241	0.4135	0.4483
HLG AV			**0.0660**	**0.0707**	**0.0989**	**0.2085**	**0.4895**	**0.3358**	**0.2785**	**0.2541**	**0.2976**	**0.3200**	**0.4087**	**0.4357**
OAV			**0.0433**	**0.0485**	**0.0836**	**0.2071**	**0.3690**	**0.2924**	**0.2645**	**0.2575**	**0.3369**	**0.3605**	**0.4796**	**0.5056**

C. THIRD SET OF EXPERIMENTS: ROBUSTNESS TO TMO

For this experiment, five TMOs are applied to the test HDR images watermarked by the HDR-IW method and the methods in [8], [9]. Namely, Clip (C-TM), Gamma (G-TM), Hable (G-TM), Mobius (M-TM) and Reinhard (R-TM) [39]. Let us recall that TMOs are designed to generate SDR images from HDR images by maintaining similar visual content. TMOs modify the contrast of an HDR image by modifying pixel values, including regions with low luma codes, which are the regions where the HDR-IW method operates. Table 6 presents the percentage of watermarked images that are assigned a Score = 4 by the observers of Experiment 3 after applying a TMO. These results show that the HDR-IW method embeds watermarks that are more robust to TMOs than those embedded by the methods in [8], [9]. Tone mapping reduces the dynamic range of an HDR image by squishing down the entire capability of representing luminance by means of luma codes. It is then expected that the watermarked

TABLE 9. BER values of the extracted binary watermarks after applying several Signal Processing Operations (SPO).

Source	ID	TF	SPO on proposed HDR-IW method				SPO on method in [8]				SPO on method in [9]			
			GN	BL	ROT	DS	GN	BL	ROT	DS	GN	BL	ROT	DS
[31]	BF_000	PQ	0.0127	0.0057	0	0.0028	0.1013	0.0492	0.0466	0.0584	0.2094	0.2066	0.3640	0.2071
	FP_230	PQ	0.0380	0.0049	0.0011	0.0055	0.0707	0.0280	0.0324	0.032	0.2105	0.2067	0.3636	0.2071
	SG_134	PQ	0.0087	0.0198	0.0041	0.0167	0.1045	0.0460	0.0482	0.0589	0.2119	0.2067	0.3629	0.2072
	SG_154	PQ	0.0121	0.0041	0.0012	0.0022	0.1809	0.1192	0.0834	0.1374	0.2125	0.2067	0.3626	0.2071
[32]	bf_3660	PQ	0.0643	0.0142	0.0030	0.0088	0.1554	0.1217	0.0713	0.1235	0.2081	0.2066	0.3643	0.2071
	cf_6640	PQ	0.0001	0.0049	0	0.0031	0.6539	0.6559	0.3009	0.6542	0.2116	0.2066	0.3628	0.2071
	cf_7400	PQ	0	0.0212	0.0055	0.0298	0.186	0.1557	0.0855	0.1594	0.2086	0.2066	0.3640	0.2071
	hdr_3335	PQ	0.1037	0.0069	0	0.0044	0.0715	0.0325	0.0328	0.0361	0.2087	0.2066	0.3640	0.2072
	sg_5636	PQ	0.0211	0.0051	0.0008	0.0038	0.1445	0.1091	0.0664	0.1121	0.2092	0.2066	0.3638	0.2071
[33]	EBU_4272	PQ	0.0036	0.0238	0	0.0180	0.1980	0.2019	0.0911	0.202	0.4135	0.3431	0.1903	0.3616
PQ AV			**0.0198**	**0.0133**	**0.0009**	**0.0107**	**0.1867**	**0.1519**	**0.0859**	**0.1574**	**0.2304**	**0.2203**	**0.3462**	**0.2226**
[34]	bbc1_012	HLG	0.1114	0.0045	0.0005	0.0045	0.066	0.0180	0.0304	0.0200	0.3767	0.3672	0.2872	0.3724
	bbc1_306	HLG	0.0700	0.0144	0.0043	0.0171	0.0560	0.0047	0.0257	0.0074	0.3548	0.3344	0.2974	0.3437
	bbc1_435	HLG	0.0351	0.0092	0	0.0088	0.0641	0.0055	0.0294	0.0091	0.3243	0.3220	0.3114	0.3245
[35]	bbcc1_005	HLG	0.0595	0.0377	0.0152	0.0457	0.0457	0.0034	0.021	0.0043	0.4096	0.3470	0.2720	0.3634
	bbcc1_048	HLG	0.0575	0.0520	0.0226	0.0554	0.0700	0.0116	0.0323	0.0160	0.3134	0.2956	0.3165	0.3022
	bbcc1_066	HLG	0.0501	0.0176	0.0051	0.0196	0.0744	0.0068	0.0342	0.0127	0.4109	0.4086	0.2715	0.4108
[36]	bbcc2_031	HLG	0.0502	0.0172	0.0064	0.0206	0.0646	0.0124	0.0297	0.0174	0.2533	0.2332	0.3442	0.2401
	bbcc2_045	HLG	0.0867	0.0113	0.0030	0.0117	0.0776	0.0198	0.0357	0.0271	0.2575	0.2333	0.3423	0.2415
	bbcc2_092	HLG	0.0520	0.1010	0.0439	0.1028	0.0538	0.0039	0.0247	0.0060	0.3530	0.3225	0.2981	0.3337
	bbcc2_095	HLG	0.1000	0.0701	0.0099	0.0659	0.0522	0.0039	0.0239	0.0055	0.2609	0.2435	0.3406	0.2500
HLG AV			**0.0674**	**0.0317**	**0.0106**	**0.0335**	**0.0624**	**0.0090**	**0.0287**	**0.0126**	**0.3314**	**0.3107**	**0.3081**	**0.3182**
OAV			**0.0424**	**0.0225**	**0.0058**	**0.0221**	**0.1246**	**0.0805**	**0.0573**	**0.0850**	**0.2809**	**0.2655**	**0.3272**	**0.2704**

images by the HDR-IW method with low $\widehat{luma}_{ER}$ values be assigned the full imperceptibility score (4) after applying a TMO.

To quantitatively evaluate the robustness to TMOs, we use the Bit Error Rate between the original binary watermark, BW, and the tone-mapped binary watermark, $\widehat{BW}$:

$$BER = \frac{1}{m \cdot n} \sum_{i=1}^{m} \sum_{j=1}^{n} \left| BW_{i,j} - \widehat{BW}_{i,j} \right| \in [0, 1] \qquad (14)$$

BER values are tabulated in Table 7 for 20 of the most representative test HDR images in terms of color distribution, texture, variety of lighting conditions, and dominant contrast proportions. These results show that the HDR-IW method is more robust to TMOs than the methods in [8], [9], as BER values attained by this method are the lowest for all TMOs. It is important to recall that the HDR-IW method embeds the watermark in low luminance regions, whose values are less susceptible to aggressive tone mapping. Note that the method in [9] is particularly susceptible to TMOs for PQ-encoded images, with an average BER as high as 0.5036.

Figure 20 shows sample binary watermarks extracted after applying a TMO to the HDR images watermarked by the HDR-IW method and the methods in [8], [9]. These visual results confirm the trend observed in the BER values tabulated in Table 7. Specifically, note that although the binary watermarks for the HDR-IW method have noticeable visual artifacts, they have a higher visual quality than those for the methods in [8], [9].

D. FOURTH SET OF EXPERIMENTS: ROBUSTNESS TO LOSSY COMPRESSION

To evaluate the robustness to lossy compression, we use the HEVC compression standard reference software HM v.16.18 [40], which supports HDR compression. We employ intra-prediction coding with four different Quantization Parameters (QP), ranging from a low compression level, $QP = 0$, to a very high compression level, $QP = 40$.

Table 8 tabulates the BER values of the decoded binary watermarks w.r.t. the original binary watermark after lossy compression, using the proposed HDR-IW and the methods in [8], [9]. As expected, these results show that the robustness of all methods to lossy compression decreases as the compression is more aggressive. This is due to the fact that lossy compression mechanisms tend to compress more aggressively smooth regions, which are where watermarks are usually embedded in the pixel domain. When aggressive lossy compression is used, e.g., $QP = 40$, the maximum BER value for the HDR-IW method is 0.2840. Conversely, the maximum BER value for the methods in [8], [9] for $QP = 40$ are 0.7236 and 0.7246, respectively. We acknowledge that the sensitivity to aggressive lossy compression is one aspect of the proposed HDR-IW that may limit its applicability for the distribution of HDR images in compressed format.

E. FIFTH SET OF EXPERIMENTS: ROBUSTNESS TO COMMON SIGNAL PROCESSING OPERATIONS

Watermarks embedded in the spatial domain can be easily modified by applying common signal processing operations such as noise addition (GN), blurring (BL), rotation (ROT) and downscaling (DS). To measure the robustness to these common operations, we modify the test watermarked images, as follows:

1) GN: Gaussian white noise is added to the Y-channel with a variance = 0.01.
2) BL: Blurring effects are introduced by replicating the border pixel values.

FIGURE 20. Binary watermarks extracted from BF_000 (Rec.2020 + PQ OETF) after applying various TMOs. (Left to right) TMO: C-TM, G-TM, H-TM, M-TM, R-TM. First row: proposed HDR-IW method. Second row: method in [8]. Third row: method in [9].

3) ROT: The image is rotated by 45° w.r.t the original position.
4) DS: The image is down-scaled by a factor of 0.5.

Table 9 shows the BER values of the binary watermarks w.r.t. the original binary watermark after applying the signal processing operations listed before. These results confirm that the HDR-IW method is very robust to such operations. The largest BER values are obtained after adding Gaussian white noise; however, the average BER value for this operation is below 0.05. The methods in [8], [9] tend to be, on average, also robust to these signal processing operations. However, in general, the BER values for these methods are larger than those for the proposed method.

We finish this section with some comments about the computational complexity of the proposed HDR-IW method. For the evaluated HDR images tabulated in Table 2, our method takes, on average, 12.26 seconds to watermark each image on a PC with an Intel Core i7-7500U @2.90GHz CPU and 16GB of RAM. The methods in [8], [9] take, on average, 734.54 and 84.90 seconds, respectively, to watermark each of these HDR images on the same computer. Such low average processing times make the proposed method very well-suited and applicable for real-life scenarios.

VI. CONCLUSION

In this paper, we proposed the HDR-IW method to protect HDR images by embedding binary watermarks in the spatial domain that are imperceptible to the HVS. The HDR-IW method is based on a thorough analysis of the modelling used by an OETF to represent HDR images as a non-linear digital signal, the linear luminance radiated by an HDR screen by means of an EOTF, and the brightness perceived by the HVS from the HDR screen. To this end, the method uses an LVT curve to determine not only the most appropriate ER, but also the maximum variation that luma codes within the ER can tolerate before any changes can be perceived by the HVS. The watermarks embedded by the HDR-IW method in the spatial domain remain imperceptible to the HVS as long as the TF is not altered or the normal calibration and colorimetry conditions of the HDR screen remain unchanged. Our evaluations on a wide range of real-life HDR images encoded by the PQ and HLG TFs confirmed the method's capacity to embed imperceptible watermarks and its robustness to various manipulations, including tone-mapping. The HDR-IW method is then an attractive option to merge the advantages of invisible and visible watermarking methods to protect HDR imaging. Our future work focuses on increasing the robustness of the HDR-IW method to very aggressive lossy compression.

ACKNOWLEDGMENT

The authors thank the BBC Research and Development and the University of Stuttgart for providing the test HDR images.

REFERENCES

[1] D. Blackburn, J. A. Eisenach, and D. Harrison, JR., "Impacts of digital video piracy on the US Economy," 2019.

[2] C.-H. Huang, S.-C. Chuang, Y.-L. Huang, and J.-L. Wu, "Unseen visible watermarking: A novel methodology for auxiliary information delivery via visual contents," *IEEE Trans. Inf. Forensics Security*, vol. 4, no. 2, pp. 193–206, Jun. 2009.
[3] S.-C. Chuang, C.-H. Huang, and J.-L. Wu, "Unseen visible watermarking," in *Proc. IEEE Int. Conf. Image Process.*, vol. 3, Sep./Oct. 2007, p. III-261.
[4] K. Perez-Daniel, F. Garcia-Ugalde, and V. Sanchez, "Scene-based imperceptible-visible watermarking for HDR video content," in *Proc. 7th Int. Workshop Biometrics Forensics (IWBF)*, May 2019, pp. 1–6.
[5] K. R. Perez-Daniel and V. Sanchez, "Luma-aware multi-model rate-control for HDR content in HEVC," in *Proc. IEEE Int. Conf. Image Process. (ICIP)*, Sep. 2017, pp. 1022–1026.
[6] A. O. Zaid and A. Houimli, "HDR image compression with optimized JPEG coding," in *Proc. 25th Eur. Signal Process. Conf. (EUSIPCO)*, Aug. 2017, pp. 1539–1543.
[7] D. Kobayashi, K. Nakamura, T. Onishi, H. Iwasaki, and A. Shimizu, "A 4K/60p HEVC real-time encoding system with high quality HDR color representations," *IEEE Trans. Consum. Electron.*, vol. 64, no. 4, pp. 433–441, Nov. 2018.
[8] F. Yazdan Bakhsh and M. E. Moghaddam, "A robust HDR images watermarking method using artificial bee colony algorithm," *J. Inf. Secur. Appl.*, vol. 41, pp. 12–27, Aug. 2018.
[9] E. Maiorana and P. Campisi, "Multi-bit watermarking of high dynamic range images based on perceptual models," *Secur. Commun. Netw.*, vol. 9, no. 8, pp. 705–720, May 2016.
[10] F. Guerrini, M. Okuda, N. Adami, and R. Leonardi, "High dynamic range image watermarking robust against tone-mapping operators," *IEEE Trans. Inf. Forensics Security*, vol. 6, no. 2, pp. 283–295, Jun. 2011.
[11] F. Autrusseau and D. Goudia, "Non linear hybrid watermarking for high dynamic range images," in *Proc. IEEE Int. Conf. Image Process.*, Sep. 2013, pp. 4527–4531.
[12] E. Maiorana, V. Solachidis, and P. Campisi, "Robust multi-bit watermarking for HDR images in the radon-DCT domain," in *Proc. 8th Int. Symp. Image Signal Process. Anal. (ISPA)*, Sep. 2013, pp. 284–289.
[13] Y. Bai, G. Jiang, M. Yu, Z. Peng, and F. Chen, "Towards a tone mapping-robust watermarking algorithm for high dynamic range image based on spatial activity," *Signal Process., Image Commun.*, vol. 65, pp. 187–200, Jul. 2018.
[14] T. Luo, G. Jiang, M. Yu, H. Xu, and W. Gao, "Robust high dynamic range color image watermarking method based on feature map extraction," *Signal Process.*, vol. 155, pp. 83–95, Feb. 2019.
[15] V. Solachidis, E. Maiorana, P. Campisi, and F. Banterle, "HDR image watermarking based on bracketing decomposition," in *Proc. 18th Int. Conf. Digit. Signal Process. (DSP)*, Jul. 2013, pp. 1–6.
[16] C. Rattanacharuchinda and T. Amornraksa, "Image watermarking for high dynamic range images," in *Proc. 9th Int. Conf. Electr. Eng./Electron., Comput., Telecommun. Inf. Technol.*, May 2012, pp. 1–4.
[17] W.-F. Hsieh and P.-Y. Lin, "Imperceptible visible watermarking scheme using color distribution modulation," in *Proc. 9th Int. Conf. Ubiquitous Intell. Comput. 9th Int. Conf. Autonomic Trusted Comput.*, Sep. 2012, pp. 1002–1005.
[18] P.-Y. Lin, "Imperceptible visible watermarking based on postcamera histogram operation," *J. Syst. Softw.*, vol. 95, pp. 194–208, Sep. 2014.
[19] O. Juarez-Sandoval, E. Fragoso-Navarro, M. Cedillo-Hernandez, A. Cedillo-Hernandez, M. Nakano, and H. Perez-Meana, "Improved imperceptible visible watermarking algorithm for auxiliary information delivery," *IET Biometrics*, vol. 7, no. 4, pp. 305–313, Jul. 2018.
[20] *High Dynamic Range Electro-Optical Transfer Function of Mastering Reference Displays*, SMPTE Standard 2084, Aug. 2014, pp. 1–14.
[21] T. Borer and A. Cotton, "A 'display independent' high dynamic range television system," *SMPTE Motion Imag. J.*, vol. 125, no. 4, pp. 50–56, 2016.
[22] S. Hecht, C. Haig, and A. M. Chase, "The influence of light adaptation on subsequent dark adaptation of the eye," *J. Gen. Physiol.*, vol. 20, no. 6, pp. 831–850, Jul. 1937.
[23] P. Barten, "Formula for the contrast sensitivity of the human eye," *Proc. SPIE*, vol. 5294, pp. 231–238, Dec. 2003.
[24] M. Cowan, G. Kennel, T. Maier, and B. Walker, "Contrast sensitivity experiment to determine the bit depth for digital cinema," *SMPTE Motion Imag. J.*, vol. 113, no. 9, pp. 281–292, Sep. 2004.
[25] B. M. Hemminger, R. E. Johnston, J. P. Rolland, and K. E. Muller, "Introduction to perceptual linearization of video display systems for medical image presentation," *J. Digit. Imag.*, vol. 8, no. 1, pp. 21–34, Feb. 1995.
[26] V. Jakhetiya, W. Lin, S. Jaiswal, K. Gu, and S. C. Guntuku, "Just noticeable difference for natural images using RMS contrast and feed-back mechanism," *Neurocomputing*, vol. 275, pp. 366–376, Jan. 2018.
[27] *Image Parameter Values for High Dynamic Range Television for Use in Production and International Programme Exchange*, Recommendation document ITU-R BT.2100-2, 2018.
[28] R. Achanta, A. Shaji, K. Smith, A. Lucchi, P. Fua, and S. Süsstrunk, "SLIC superpixels compared to State-of-the-Art superpixel methods," *IEEE Trans. Pattern Anal. Mach. Intell.*, vol. 34, no. 11, pp. 2274–2282, Nov. 2012.
[29] S. K. Mitra, M. K. Kundu, C. A. Murthy, B. B. Bbattacharya, and T. Acharya, "Digital watermarking using homogeneity in image," in *Proc. Conf. Convergent Technol. Asia–Pacific Region (TENCON)*, vol. 3, 2003, pp. 944–948.
[30] L. L. Si, F. X. Sang, and Z. Liu, "Research on dot gain compensation curve algorithm model," *Appl. Mech. Mater.*, vol. 200, pp. 627–631, Oct. 2012.
[31] J. Froehlich, S. Grandinetti, B. Eberhardt, S. Walter, A. Schilling, and H. Brendel, "Creating cinematic wide gamut HDR-video for the evaluation of tone mapping operators and HDR-displays," *Proc. SPIE*, vol. 9023, pp. 279–288, Mar. 2014, doi: 10.1117/12.2040003.
[32] Stuttgart University. *High Dynamic Range Database Graded MPEG Teaser Clips*. Accessed: Apr. 7, 2020. [Online]. Available: https://hdr-2014.hdm-stuttgart.de/
[33] EBU-SVT. *Public HDR Test Sequences*. Accessed: Apr. 7, 2020. [Online]. Available: https://tech.ebu.ch/EBU_SVT_Public_Test_Sequences
[34] *BBC Hybrid Log Gamma High Dynamic Range Demonstration File Pack. Demonstration File*, BBC R&D, Greater Manchester, U.K., 2017.
[35] *BBC Hybrid Log Gamma High Dynamic Range Demonstration File Pack. Demonstration File, Complementary File 1*, BBC R&D, Greater Manchester, U.K., 2017.
[36] *BBC Hybrid Log Gamma High Dynamic Range Demonstration File Pack. Demonstration File, Complementary File 2*, BBC R&D, Greater Manchester, U.K., 2017.
[37] R. Mantiuk, K. J. Kim, A. G. Rempel, and W. Heidrich, "HDR-VDP-2: A calibrated visual metric for visibility and quality predictions in all luminance conditions," *ACM Trans. Graph.*, vol. 30, no. 4, pp. 1–14, Jul. 2011.
[38] J. Munkberg, P. Clarberg, J. Hasselgren, and T. Akenine-Möller, "High dynamic range texture compression for graphics hardware," *ACM Trans. Graph.*, vol. 25, no. 3, pp. 698–706, 2006.
[39] FFMPEG Multimedia Framework. *FFMPEG v4.0.2*. Accessed: Apr. 7, 2020. [Online]. Available: https://www.ffmpeg.org/
[40] High Efficiency Video Coding (HEVC) Software *HM v16.18*. Accessed: Apr. 7, 2020. [Online]. Available: https://hevc.hhi.fraunhofer.de/svn/svn_HEVCSoftware/

KARINA RUBY PEREZ-DANIEL (Member, IEEE) received the B.S. degree in electronics and telecommunications from the Autonomous University of the State of Hidalgo, in 2008, and the M.Sc. degree in microelectronics engineering and the Ph.D. degree in communications and electronics from the National Polytechnic Institute (IPN), Mexico, in 2010 and 2015, respectively. In 2014, she was a Research Intern with Microsoft Research. In 2016, she collaborates as a Postdoctoral Fellow with the University of Warwick. From 2017 to 2018, she was a Postdoctoral Fellow with the Autonomous National University of Mexico (UNAM). She is currently a Full-Time Professor with the Engineering Faculty, Universidad Panamericana. Her principal research interests include image and video processing, object detection, computer vision, video coding, watermarking, and artificial intelligence.

FRANCISCO GARCIA-UGALDE was born in Mexico. He received the bachelor's degree in electronics and electrical system engineering from the National Autonomous University of Mexico, in 1977, the Diplome d'Ingénieur degree from SUPELEC, France, in 1980, and the Ph.D. degree in information processing from the Université de Rennes I, France, in 1982. Since 1983, he has been a Full-Time Professor with the National Autonomous University of Mexico. His research interests include video coding, image analysis, watermarking, theory and applications of error control coding, turbo coding, applications of cryptography, and parallel processing and data bases.

VICTOR SANCHEZ (Member, IEEE) received the M.Sc. degree from the University of Alberta, Canada, in 2003, and the Ph.D. degree from The University of British Columbia, Canada, in 2010. From 2011 to 2012, he was with the Video and Image Processing Laboratory, University of California at Berkeley, as a Postdoctoral Researcher. In 2012, he was a Visiting Lecturer with the Group on Interactive Coding of Images, Universitat Autonoma de Barcelona. From 2018 to 2019, he was a Visiting Scholar with the School of Electrical and Information Engineering, The University of Sydney, Australia. He is currently an Associate Professor with the Department of Computer Science, University of Warwick, U.K. His research has been funded by the Consejo Nacional de Ciencia y Tecnologia, Mexico, the Natural Sciences and Engineering Research Council, Canada, the Canadian Institutes of Health Research, the FP7 and the H2020 Programs of the European Union, the Engineering and Physical Sciences Research Council, U.K., and the Defence and Security Accelerator, U.K. He has authored several technical articles, book chapters, and a book in these areas. His main research interests include signal and information processing with applications to multimedia analysis and image and video coding, security, and communications.